Phagocytosis and self-destruction execute dendrite degeneration of *Drosophila* sensory neurons at distinct levels of NAD^+ reduction

Hui Ji[1,3], Maria L. Sapar[1,2,3], Ankita Sarkar[1], Bei Wang[1], and Chun Han[1*]

[1]Weill Institute for Cell and Molecular Biology and Department of Molecular Biology and Genetics, Cornell University, Ithaca, NY 14853, USA

[2]Current address: New York Stem Cell Foundation, New York, NY 10019, USA

[3]These authors contributed equally to this work

*Correspondence and Lead Contact: chun.han@cornell.edu

RUNNING TITLE

NAD^+ reduction coordinates PS-mediated phagocytosis and self-destruction of dendrites

Keywords

phosphatidylserine, PS exposure, phagocytosis, phagocyte, self-destruction, Wallerian degeneration, dendrite degeneration, NAD^+, Nmnat, Sarm, Axed, calcium, *Drosophila*, da neuron

ABSTRACT

After injury, severed dendrites and axons expose the "eat-me" signal phosphatidylserine (PS) on their surface and degenerate by disassembly. While axon degeneration is controlled by a conserved "axon-death" pathway that is thought to activate self-destruction, how PS exposure is regulated by this pathway and whether PS-induced phagocytosis contributes to neurite breakdown *in vivo* remain unknown. Here we show that in *Drosophila* sensory dendrites, PS exposure and self-destruction are triggered by two distinct levels of NAD^+ reduction downstream of Sarm activation. Surprisingly, phagocytosis is the main driver of dendrite degeneration induced by both genetic NAD^+ disruptions and injury. Furthermore, the axon-death factor Axed is only partially required for self-destruction of injured dendrites, acting in parallel with PS-induced phagocytosis. Lastly, injured dendrites exhibit a unique rhythmic calcium flashing that correlates with self-destruction. Therefore, a special genetic program coordinates PS exposure and self-destruction in injury-induced dendrite degeneration *in vivo*.

INTRODUCTION

Physical insults to the nervous system often disrupt neuronal connectivity and function by damaging dendritic or axonal processes of neurons. Injured axons break down through a series of stereotypical events collectively called Wallerian degeneration (WD) (Coleman and Freeman, 2010; Waller, 1850). Dendrites undergo a similar program of degeneration after injury (Tao and Rolls, 2011). Before neurons can regenerate their processes and restore connections, the debris from damaged neurites has to be promptly cleared by phagocytes, which are cells that engulf dead cells or cell debris (Sapar and Han, 2019). Inefficient clearance can lead to neuroinflammation and further exacerbate the damage to the surrounding tissues (Davies et al., 2019; Galloway et al., 2019). Although WD is mainly considered to be a neurite-intrinsic, self-destructive process (Gerdts et al., 2016), whether phagocytosis actively contributes to degeneration of injured neurites *in vivo*, rather than merely passively removing neuronal debris, remains unclear.

WD is governed by an evolutionarily conserved pathway, which is also called "axon-death" pathway because it was discovered in studies focused primarily on axon degeneration in *Drosophila* and rodents (Freeman et al., 2003; Gerdts et al., 2016; Sapar and Han, 2019). This pathway is centered on nicotinamide adenine dinucleotide (NAD^+), an essential cellular

46 metabolite that is locally depleted after axons are injured. The signaling cascade starts with
47 injury-induced activation of the E3 ubiquitin ligase Highwire/Phr1 in severed axons (Babetto et
48 al., 2013; Xiong et al., 2012), which in turn causes degradation of nicotinamide mononucleotide
49 adenyltransferase (Nmnat), an enzyme required for the synthesis of NAD^+ (Zhai et al., 2009).
50 The resultant decrease of NAD^+ levels (Sasaki et al., 2016), together with an accumulation of the
51 NAD^+ precursor nicotinamide mononucleotide (NMN) (Di Stefano et al., 2015; Liu et al., 2018),
52 activates Sarm/SARM1, a sterile alpha/Armadillo/Toll-Interleukin receptor homology domain
53 protein (Bratkowski et al., 2020; Figley et al., 2021; Jiang et al., 2020; Osterloh et al., 2012;
54 Shen et al., 2021). Sarm/SARM1 carries NADase activity; thus its activation causes catastrophic
55 NAD^+ depletion, which drives axon breakdown through unclear mechanisms (Gerdts et al.,
56 2015; Wang et al., 2005).

57 Besides this core Highwire/Phr1-Nmnat-NAD^+-Sarm/SARM1 pathway, several other
58 factors have also been found to act in WD. Downstream of *Sarm*, *axundead* (*axed*) is required for
59 axon degeneration of olfactory receptor neurons (ORNs) and wing sensory neurons in
60 *Drosophila* (Neukomm et al., 2017). The loss of *axed* blocks axon degeneration even when Sarm
61 is dominantly activated, raising the possibility that Axed activation, rather than NAD^+ depletion,
62 is the key switch of WD (Neukomm et al., 2017). In addition, *pebbled* (*peb*) encodes a
63 *Drosophila* transcription factor required for axon degeneration of glutamatergic but not
64 cholinergic sensory neurons in the wing (Farley et al., 2018). Lastly, the dual leucine kinase
65 (DLK)/c-Jun N-terminal kinase (JNK) stress pathway also contributes to, but is not required for,
66 WD in both *Drosophila* and mice (Miller et al., 2009; Yang et al., 2015). Although how these
67 factors interact with the core pathway to promote axon degeneration is still mysterious, it is
68 generally believed that catastrophic NAD^+ depletion caused by Sarm activity initiates a neurite-
69 intrinsic self-destruction program that ultimately is responsible for WD of axons (Babetto et al.,
70 2013; Gerdts et al., 2015; Gerdts et al., 2016; Neukomm et al., 2017). While the WD pathway is
71 primarily characterized in axons, evidence suggests that NAD^+ reduction is also an essential step
72 in injury-induced dendrite degeneration (Sapar et al., 2018; Tao and Rolls, 2011). However,
73 which components of the WD pathway are conserved in dendrites remains unknown.

74 Neuronal debris is recognized by resident phagocytes of the nervous system through
75 specific "eat-me" signals exposed on the neuronal surface. A highly conserved eat-me signal is
76 phosphatidylserine (PS), a negatively charged phospholipid normally found in the inner leaflet of

77 the plasma membrane of healthy cells. During apoptosis, PS is externalized to the outer leaflet of
78 the plasma membrane to mark the cell for engulfment (Leventis and Grinstein, 2010). Genetic
79 analyses of certain PS-binding bridging molecules and cell membrane receptors in mice and
80 zebrafish suggest that PS recognition contributes to the phagocytosis of neurons (Fourgeaud et
81 al., 2016; Mazaheri et al., 2014; Nandrot et al., 2007). Similarly, clearance of injured axons and
82 dendrites in *Drosophila* requires Draper (Drpr), an engulfment receptor that binds to PS
83 (Freeman et al., 2003; Han et al., 2014; MacDonald et al., 2006; Tung et al., 2013). PS exposure
84 has also been directly observed on injured axons of mouse neurons *in vitro* (Shacham-Silverberg
85 et al., 2018; Sievers et al., 2003) and on injured dendrites of *Drosophila* sensory neurons *in vivo*
86 (Sapar et al., 2018). Although axonal PS exposure can be induced independent of axon
87 degeneration *in vitro* (Shacham-Silverberg et al., 2018), ectopically induced PS exposure
88 resulted in engulfment-dependent neurite reduction of otherwise healthy neurons in both the
89 central nervous system (CNS) and the peripheral nervous system (PNS) of *Drosophila* (Sapar et
90 al., 2018), pointing to a dominant effect of PS exposure in induced phagocytosis. Recent studies
91 revealed a link between neuronal PS exposure and the WD pathway. Overexpression of Wld^S, a
92 fusion protein containing the full-length murine Nmnat1 (Mack et al., 2001), in *Drosophila*
93 sensory neurons suppresses PS exposure of injured dendrites (Sapar et al., 2018). In addition,
94 *Sarm1* ablation and NAD^+ supplementation in neuronal culture reduce PS exposure on injured
95 axons (Shacham-Silverberg et al., 2018). These observations raise two important questions: How
96 does the WD pathway regulate and coordinate both neurite PS exposure and self-destruction?
97 What are the relative contributions of PS-mediated phagocytosis and neurite self-destruction in
98 WD *in vivo*?

99 To address these questions, we utilized *Drosophila* class IV dendritic arborization (C4da)
100 neurons on the larval body wall, an established *in vivo* model of injury-induced dendrite
101 degeneration (Han et al., 2014). In this system, degenerating dendrites of C4da neurons are
102 phagocytosed by epidermal cells through the engulfment receptor Drpr. Here we show that PS
103 exposure and dendrite self-destruction are two steps activated at different levels of NAD^+
104 reduction, and that *in vivo*, phagocytosis is the main driving force of dendrite degeneration
105 induced by both genetic NAD^+ perturbations and injury. Interestingly, injury and genetic NAD^+
106 perturbations cause dendrite degeneration through different cellular mechanisms in membrane
107 disruption, dendrite calcium dynamics, and phagocytosis dependence. Furthermore, Axed

specifically promotes, but is not required for, dendrite self-destruction, suggesting different mechanisms of injury-induced degeneration in axons and dendrites. Lastly, we report a previously unknown rhythmic calcium flashing specifically in injured dendrites, which is disrupted by Wld^S overexpression and *axed* loss, indicating a potential role of calcium flashing in dendrite self-destruction.

RESULTS

Nmnat knockout induces spontaneous dendrite degeneration due to Sarm-mediated NAD^+ reduction

NAD^+ reduction is required for PS exposure on injured dendrites (Sapar et al., 2018). To determine if NAD^+ loss is also sufficient to cause neuronal PS exposure, we decided to first investigate the impact of removing *Nmnat* from C4da neurons, as the loss of *Nmnat* is expected to cause cell-autonomous NAD^+ reduction. *Nmnat* LOF is known to induce degeneration of eye photoreceptors (Zhai et al., 2006) and wing sensory neurons (Neukomm et al., 2017). However, a previous study found that C4da neurons mutant for *Nmnat* did not show dendrite degeneration, despite displaying dendrite reduction and axon degeneration (Wen et al., 2011). To reexamine the LOF phenotype of *Nmnat*, we used CRISPR-TRiM, a tissue-specific mutagenesis method we previously developed (Poe et al., 2019), to knock out *Nmnat* in C4da neurons. In this method, *Nmnat* is knocked out by C4da-specific *ppk-Cas9* and two ubiquitously expressed guide-RNAs (gRNAs) targeting *Nmnat*. To distinguish dendrite reduction caused by degeneration from that caused by growth defects, we used CD4-tdTomato (CD4-tdTom) to label C4da dendrites. Because tdTom is stable in phagosomes, the presence of tdTom-labeled dendrite debris in epidermal cells is an indication of dendrite breakdown and subsequent engulfment (Han et al., 2014).

As expected, *Nmnat* knockout (KO) in C4da neurons (Figure 1B) caused strong dendritic reduction (Figure 1G) in wandering 3rd instar larvae as compared to the control (Figures 1A). In addition, dendrite debris was observed to spread in epidermal cells underneath and near the dendrites of *Nmnat* KO neurons (Figures 1B and 1H), suggesting that some dendrites had degenerated and were engulfed by epidermal cells. Unlike degenerating dendrites observed during developmental pruning or after injury (Han et al., 2011; Han et al., 2014), the remaining dendrites of *Nmnat* KO neurons did not show obvious blebbing or fragmentation, which may

138 explain why dendrite degeneration was not detected previously in *Nmnat* mutant C4da neurons,
139 considering that the membrane GFP marker used to label dendrites in the previous study is
140 rapidly degraded by epidermal cells once engulfed and thus cannot visualize phagosomes (Han et
141 al., 2014; Wen et al., 2011).

142 Nmnat protects neurons by both synthesizing NAD^+ and functioning as a chaperon
143 protein (Ali et al., 2013). To verify that the observed dendrite degeneration is due to the loss of
144 Nmnat enzymatic activity, we tried to rescue *Nmnat* KO neurons by overexpressing Wld^S, which
145 contains full NMNAT activity (Mack et al., 2001), and $Wld^{S\text{-}dead}$, a mutant version of Wld^S that

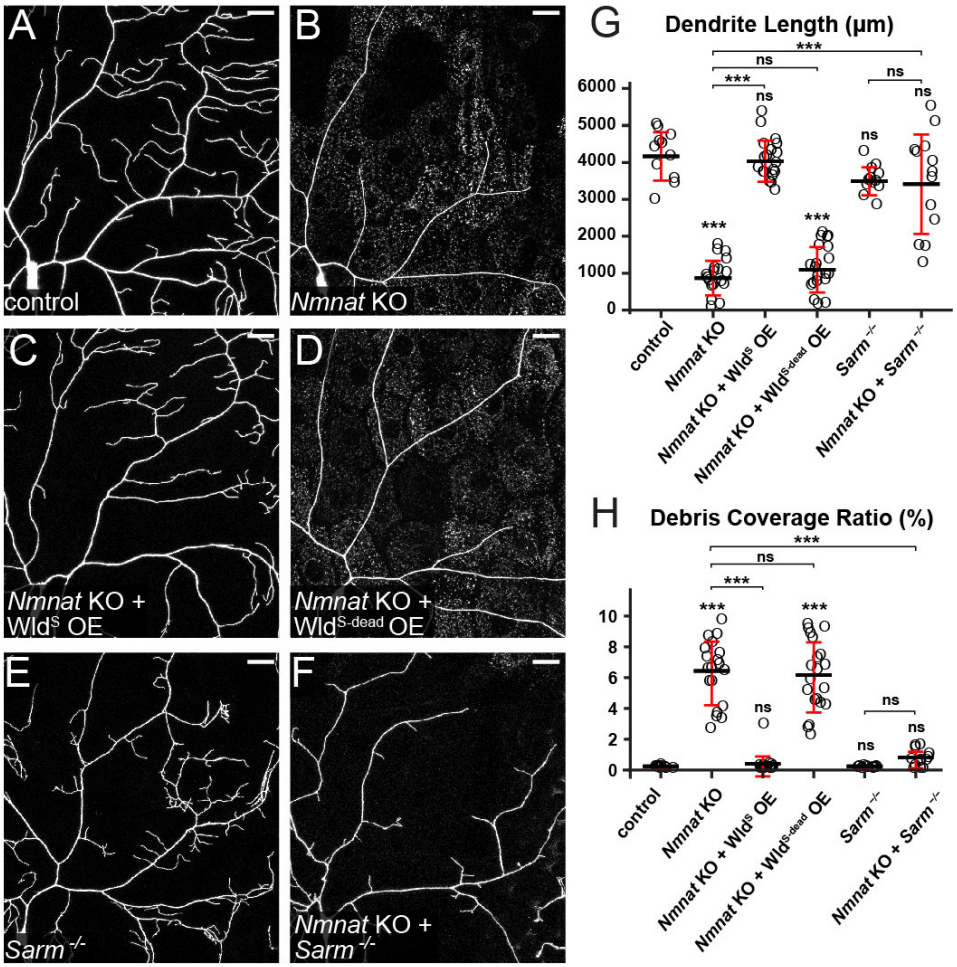

Figure 1: *Nmnat* knockout induces spontaneous dendrite degeneration due to Sarm-mediated NAD^+ reduction

(A-F) Partial dendritic fields of control (A), *Nmnat* KO (B), *Nmnat* KO + Wld^S OE (C), *Nmnat* KO + $Wld^{S\text{-}dead}$ OE (D), $Sarm^{4705/4621}$ (E), and *Nmnat* KO + $Sarm^{4705/4621}$ (F) ddaC C4da neurons. Neurons were labeled by *ppk>CD4-tdTom* (A-D) and *ppk-CD4-tdTom* (E and F). The C4da-specific KO was induced by *ppk-Cas9*. Scale bars, 25 µm.

(G) Quantification of dendrite length. n = number of neurons: control (n =11, 6 animals); *Nmnat* KO (n = 19, 10 animals); *Nmnat* KO + Wld^S OE (n = 17, 10 animals); *Nmnat* KO + $Wld^{S\text{-}dead}$ OE (n = 20, 11 animals); $Sarm^{4705/4621}$ (n = 12, 6 animals); *Nmnat* KO + $Sarm^{4705/4621}$ (n = 13, 8 animals). One-way ANOVA and Tukey's test.

(H) Quantification of debris coverage ratio, which is the percentage of debris area normalized by dendrite area ratio. Number of neurons: same as in (G). Kruskal-Wallis (One-way ANOVA on ranks) and Dunn's test, p-values adjusted with the Benjamini-Hochberg method.

For all quantifications, ***$p \leq 0.001$; n.s., not significant. The significance level above each genotype is for comparison with the control. Black bar, mean; red bar, SD.

146 cannot synthesize NAD^+ but maintains the chaperon function (Avery et al., 2009). Wld^S
147 overexpression (OE) rescued the degeneration of *Nmnat* KO neurons and restored dendrite
148 morphology to the wildtype level (Figures 1C, 1G, and 1H), while $Wld^{S\text{-}dead}$ OE did not change
149 dendrite length or debris level of *Nmnat* KO neurons (Figures 1D, 1G, and 1H). These results
150 suggest that NAD^+ reduction is responsible for the dendrite degeneration of *Nmnat* KO neurons.

151 We next asked whether Sarm plays a role in *Nmnat* KO-induced dendrite degeneration.
152 Indeed, *Sarm* LOF completely blocked dendrite degeneration of *Nmnat* KO neurons (Figures 1F,
153 1G, 1H), as evident in the absence of dendrite debris in epidermal cells. However, these neurons
154 showed more variable dendrite length (Figure 1G) compared to *Sarm* LOF alone (Figures 1E,
155 1G, and 1H), perhaps due to the loss of Nmnat chaperon function (Wen et al., 2011).
156 Importantly, these results demonstrate that *Sarm* is required for the dendrite degeneration of
157 *Nmnat* KO neurons. All the results above together suggest that *Nmnat* LOF in neurons cause
158 spontaneous dendrite degeneration through Sarm-mediated NAD^+ loss.

159 **PS exposure-mediated phagocytosis causes dendrite degeneration of *Nmnat* KO neurons**

160 To ask whether *Nmnat* KO also causes neuronal PS exposure, we used an established method to
161 visualize PS exposure on C4da dendrites. In this method, the fluorescent PS sensor GFP-Lact is
162 expressed by the larval fat body and secreted into the hemolymph (Sapar et al., 2018). As C4da
163 dendrites are largely exposed to the hemolymph, GFP-Lact labeling allows visualization of
164 dynamic PS exposure on dendrites in intact live animals (Sapar et al., 2018). We found that GFP-
165 Lact strongly labeled *Nmnat* KO neurons at distal branches that underwent degeneration (Figure
166 2B), while wildtype C4da neurons showed no labeling (Figure 2A). Interestingly, we also
167 observed weaker GFP-Lact labeling on dendrite segments that did not display obvious signs of
168 degeneration (outlined in Figure 2B), suggesting that PS exposure may precede dendrite
169 breakdown, instead of being merely a consequence of dendrite degeneration. This conclusion
170 was further corroborated by time-lapse imaging of *Nmnat* KO neurons (Video 1) and kymograph
171 analysis (Figure 2C): PS exposure (indicated by white dotted lines) occurred well ahead of
172 dendrite fragmentation (indicated by blue dotted lines).

173 As *Sarm* is required for dendrite degeneration of *Nmnat* KO neurons, we asked if Sarm
174 also regulates PS exposure in these neurons. *Nmnat* KO neurons showed no PS exposure in the

175 *Sarm* mutant background (Figure 2D), suggesting that Sarm-mediated NAD^+ reduction is also

176 responsible for inducing the observed PS exposure.

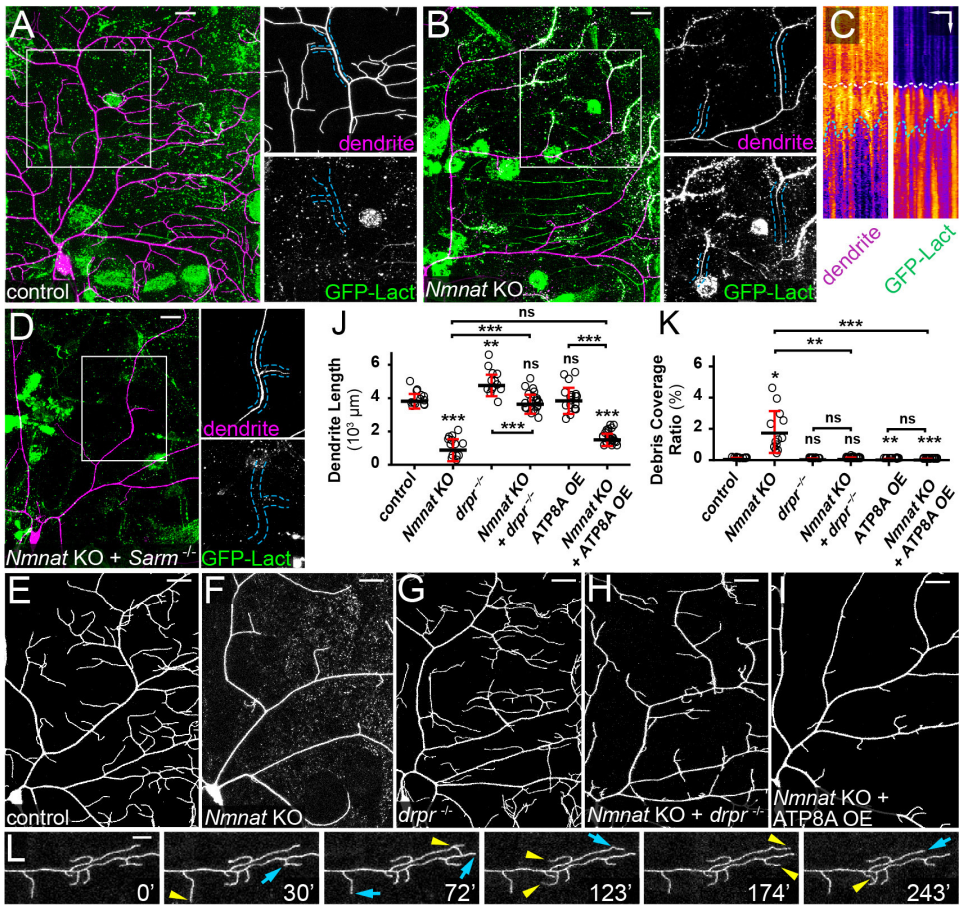

Figure 2: PS exposure-mediated phagocytosis causes dendrite degeneration of *Nmnat* KO neurons

(A) A control ddaC neuron showing the lack of GFP-Lact labeling. Insets show close-ups of an intact dendrite. Scale bar, 25 µm.

(B) A *Nmnat* KO ddaC neuron undergoing spontaneous degeneration and showing labeling by GFP-Lact. In the inset, the outlined dendrite segments do not show obvious blebbing or fragmentation but are weakly labeled by GFP-Lact. Scale bar, 25 µm.

(C) Kymographs of tdTom signal (dendrite) and GFP-Lact signal along a dendrite segment of a *Nmnat* KO ddaC neuron. White dotted lines indicate the timing of GFP-Lact initial binding to the dendrite; blue dotted lines indicate timing of the dendrite fragmentation based on the continuity of the dendrite signal. Scale bars, 10 µm horizontal, 60 min vertical. See also Video 1.

(D) Dendrites of a *Nmnat* KO + *Sarm*$^{4705/4621}$ ddaC neuron showing the lack of GFP-Lact labeling. Insets show close-ups of an intact dendrite. Scale bar, 25 µm.

(E-I) Partial dendritic fields of control (E), *Nmnat* KO (F), *drpr*$^{-/-}$ (G), *Nmnat* KO + *drpr*$^{-/-}$ (H) and *Nmnat* KO + ATP8A OE (I) neurons. Scale bars, 25 µm.

(J) Quantification of dendrite length. n = number of neurons: control (n = 13, 7 animals); *Nmnat* KO (n = 13, 7 animals); *drpr*$^{-/-}$ (n = 14, 8 animals); *Nmnat* KO + *drpr*$^{-/-}$ (n = 22, 14 animals); ATP8A OE (n=17, 9 animals); *Nmnat* KO + ATP8A OE (n=23, 9 animals). One-way ANOVA and Tukey's test.

(K) Quantification of debris coverage ratio. Number of neurons: same as in (J). Kruskal-Wallis (One-way ANOVA on ranks) and Dunn's test, p-values adjusted with the Benjamini-Hochberg method.

(L) A time series of *Nmnat* KO + *drpr*$^{-/-}$ dendrites. Yellow arrowheads indicate growth of dendrites compared to the previous frame; blue arrows indicate retractions of dendrites compared to the previous frame. Scale bar, 10 µm. See also Video 2.

In all panels, neurons were labeled by *ppk-CD4-tdTom* (A-H) and *ppk-MApHS* (I). C4da-specific KO was induced by *ppk-Cas9*. For all quantifications, *p≤0.05, **p≤0.01, ***p≤0.001; n.s., not significant. The significance level above each genotype is for comparison with the control. Black bar, mean; red bar, SD.

177 The observation of PS exposure on *Nmnat* KO dendrites raises the question of whether
178 PS exposure contributes to dendrite breakdown by inducing phagocytic attacks from epidermal
179 cells. Because PS-mediated epidermal engulfment of dendrites requires Drpr (Sapar et al., 2018),
180 we examined *Nmnat* KO dendrites in *drpr* mutant larvae. Strikingly, *drpr* LOF completely
181 blocked dendrite degeneration of *Nmnat* KO neurons (Figure 2H as compared to Figures 2E-2G;
182 Figures 2J and 2K). These dendrites exhibited dynamic extension and retraction behaviors
183 (Figure 2L and Video 2), demonstrating that they were not fragmented dendrites that failed to be
184 cleared. Next, to examine whether dendrite breakdown induced by *Nmnat* KO depends on PS
185 exposure, we tried to rescue *Nmnat* KO neurons by overexpressing ATP8A. ATP8A is the
186 *Drosophila* ortholog of PS flippase responsible for keeping PS in the inner leaflet of the plasma
187 membrane (Raiders et al., 2021; Tanaka et al., 2011), whose LOF in da neurons causes dendritic
188 PS exposure (Sapar et al., 2018). Indeed, ATP8A OE completely blocked dendrite degeneration
189 of *Nmnat* KO neurons and resulted in even less dendrite debris than the wildtype control (Figures
190 1I and 1K).

191 Thus, these data demonstrate that Sarm-mediated NAD^+ reduction causes dendrite PS
192 exposure, which in turn induces phagocytic attack to drive dendrite degeneration of *Nmnat* KO
193 neurons.

194 **Wld^S OE and *Sarm* KO suppress PS exposure and fragmentation of injured dendrites**

195 Wld^S protects injured neurites from degenerating by maintaining the NAD^+ level in the neurites.
196 We previously found that overexpressing Wld^S in C4da neurons blocked fragmentation and PS
197 exposure of ablated dendrites at 10 hrs after injury (AI) (Sapar et al., 2018). To further
198 investigate the role of the WD pathway in neuronal PS exposure, we examined the effects of
199 overexpressing Wld^S and knocking out *Sarm* in C4da neurons at 24 hrs after laser-severing of
200 dendrites. Neuronal-specific KO was conducted using *SOP-Cas9*, which is active in precursor
201 cells of da neurons, to minimize potential gene perdurance (Poe et al., 2019). As expected, Wld^S
202 OE blocked degeneration and clearance of injured dendrites also at 24 hrs AI (Figure 3C, as
203 compared to the control in Figure 3B), even though the injured arbors were greatly simplified as
204 compared to uninjured dendrites (Figures 3A and 3E). Neuronal-specific *Sarm* KO showed
205 similar effects in injured dendrites (Figures 3D and 3E) to those of Wld^S OE.

206 We next examined the effects of Wld^S OE and *Sarm* KO on dendritic PS exposure 24 hrs
207 AI. Wld^S OE prevented PS exposure on severed dendrites, even on branches that showed
208 blebbing and breakage (Figures 3F and 3I). *Sarm* KO also effectively blocked PS exposure on
209 injured dendrites (Figures 3G and 3I), with occasionally strong PS labeling on fragmented distal
210 terminal branches (Figures 3H and 3I). The above data in dendrite injury together suggest that
211 Sarm-mediated NAD$^+$ reduction causes both PS exposure and degeneration of injured dendrites.

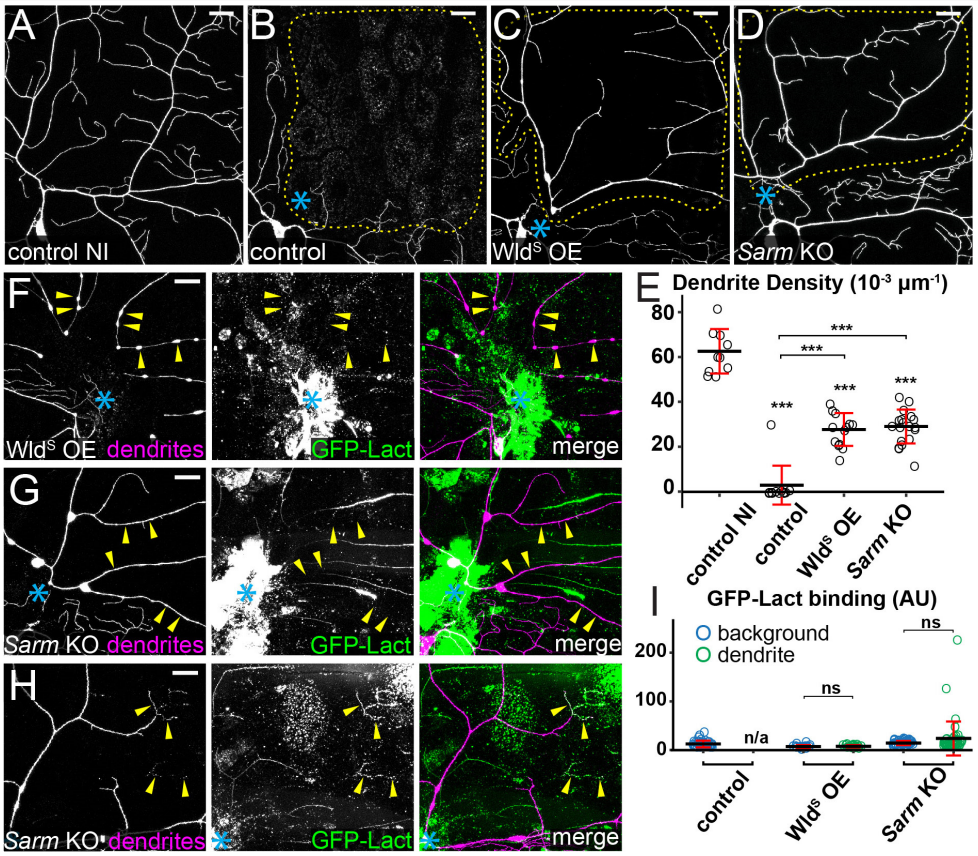

Figure 3: Wld^S OE and *Sarm* KO suppress PS exposure and fragmentation of injured dendrites

(A) Partial dendritic field of an uninjured ddaC control neuron.

(B-D) Partial dendritic fields of control (B), Wld^S OE (C) and *Sarm* KO (D) ddaC neurons 24 hrs after injury (AI). Blue asterisk, injury site. Yellow dots outline regions covered by injured dendrites.

(E) Quantification of dendrite density (1000 x dendritic length/area) in regions covered by injured dendrites. n = number of neurons: control no injury (NI) (n = 10, 10 animals); control (n = 12, 6 animals); Wld^S OE (n = 13, 6 animals); *Sarm* KO (n = 19, 6 animals).

(F and G) Wld^S OE (F) and *Sarm* KO (G) ddaC neurons 24 hrs AI, showing unfragmented dendrites and lack of GFP-Lact binding to severed dendrites (yellow arrowheads).

(H) Dendrites of a *Sarm* KO ddaC neuron 24 hrs AI, showing infrequent GFP-Lact binding at fragmented terminal branches (yellow arrowheads).

(I) Quantification of GFP-Lact binding on injured dendrites. The GFP-Lact intensity is shown for both background epidermal regions and injured dendrites. The outliers in *Sarm* KO dendrite dataset correspond to infrequent degenerating terminal branches. Background: epidermal regions without dendrites. n = number of measurements: control background (n = 39) and control dendrite (n/a, no remaining dendrites), 7 animals; Wld^S OE background (n = 18) and Wld^S OE dendrite (n = 18), 4 animals; *Sarm* KO background (n = 48) and *Sarm* KO dendrite (n = 48), 9 animals.

In all panels, neurons were labeled by *ppk-MApHS* (A-C; only tdTom channel is shown), *ppk>CD4-tdTom* (D), and *ppk-CD4-tdTom* (F-H). Neuronal-specific KO was induced by *SOP-Cas9*. For all quantifications, One-way ANOVA and Tukey test; ***p≤0.001; n.s., not significant; n/a., not applicable. The significance level above each genotype in (E) is for comparison with the control. Black bar, mean; red bar, SD. Scale bars, 25 µm.

212 The PS exposure on fragmented terminal dendrites of *Sarm* KO neurons could be due to
213 relatively faster NAD^+ turnover in those local branches even in the absence of Sarm.

214 **Ectopic PS exposure causes injured dendrites of Wld^S OE and *Sarm* KO neurons to**
215 **degenerate**

216 The absence of PS exposure on injured dendrites of Wld^S OE and *Sarm* KO neurons raises the
217 question of whether the degeneration defects of these neurons are due to the lack of PS-mediated
218 epidermal attack on dendrites. To test this hypothesis, we ectopically induced neuronal PS
219 exposure by knocking out *CDC50*, which encodes a chaperone necessary for the function of
220 *Drosophila* flippases (Tanaka et al., 2011), and by overexpressing TMEM16F, a mammalian PS
221 scramblase (Segawa et al., 2011). These manipulations in C4da neurons cause mild but
222 appreciable phagocytosis-dependent dendrite loss (Sapar et al., 2018). *CDC50* KO or TMEM16F
223 OE alone in Wld^S OE neurons caused partial or complete degeneration of injured dendrites and
224 the accompanying epidermal engulfment (Figures 4A, 4B, and 4E). A much stronger effect was
225 observed when *CDC50* KO and TMEM16F OE were combined in Wld^S OE neurons:

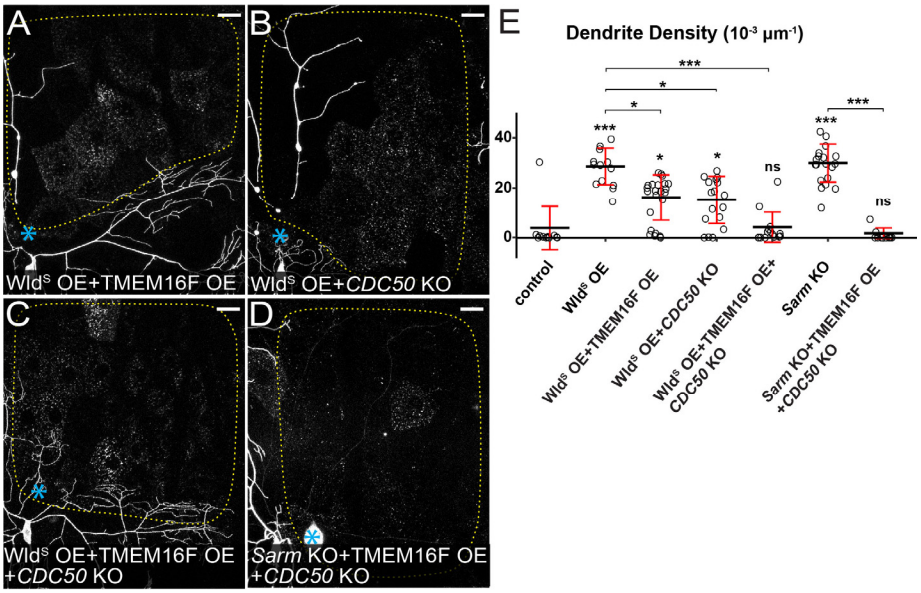

Figure 4: Ectopic PS exposure causes injured dendrites of Wld^S OE and *Sarm* KO neurons to degenerate.

(A-D) Partial dendritic fields of Wld^S OE + TMEM16F OE (A), Wld^S OE + *CDC50* KO (B), Wld^S OE + TMEM16F OE + *CDC50* KO (C) and *Sarm* KO + TMEM16F OE + *CDC50* KO (D) ddaC neurons 24 hrs AI. Blue asterisk, injury site. Yellow dots outline regions covered by injured dendrites. Neurons were labeled by *ppk-MApHS* (A, B, and C) and *ppk-CD4-tdTom* (D). Neuronal-specific KO was induced by *ppk-Cas9* (B and C) and *SOP-Cas9* (D). Scale bars, 25 µm.

(E) Quantification of dendrite density. n = number of neurons: control (n = 12, 6 animals); Wld^S OE (n = 13, 6 animals); Wld^S OE + TMEM16F OE (n = 23, 8 animals); Wld^S OE + *CDC50* KO (n = 17, 8 animals); Wld^S OE + TMEM16F OE + *CDC50* KO (n = 16, 8 animals); *Sarm* KO (n = 19, 6 animals); *Sarm* KO + TMEM16F OE + *CDC50* KO (n = 13, 7 animals). Kruskal-Wallis (One-way ANOVA on ranks) and Dunn's test, p-values adjusted with the Benjamini-Hochberg method. The dataset for Wld^S OE and *Sarm* KO is the same as in Figure 3E.

For all quantifications, *$p \leq 0.05$, ***$p \leq 0.001$; n.s., not significant. The significance level above each genotype is for comparison with the control. Black bar, mean; red bar, SD.

226 Degeneration and clearance of injured dendrites were restored to the wildtype level (Figures 4C
227 and 4E). Similarly, *CDC50* KO and TMEM16F OE caused injured dendrites of *Sarm* KO
228 neurons to completely degenerate (Figures 4D and 4E). Because injury induces a more rapid and
229 stronger PS exposure on dendrites than *CDC50* KO or TMEM16F OE (Sapar et al., 2018), our
230 data strongly suggest that injury-induced PS exposure is a major driver of dendrite breakdown by
231 activating phagocytic attack by epidermal cells.

232 **Injury and NAD$^+$ depletion cause phagocytosis-independent dendrite self-destruction**

233 Although PS-mediated phagocytosis is sufficient to break down injured dendrites, blocking
234 phagocytosis with *drpr* LOF failed to prevent the fragmentation of injured dendrites 20 hrs AI,
235 even though the dendrite debris was left unengulfed (Figures 5A-5C). A neurite self-destruction

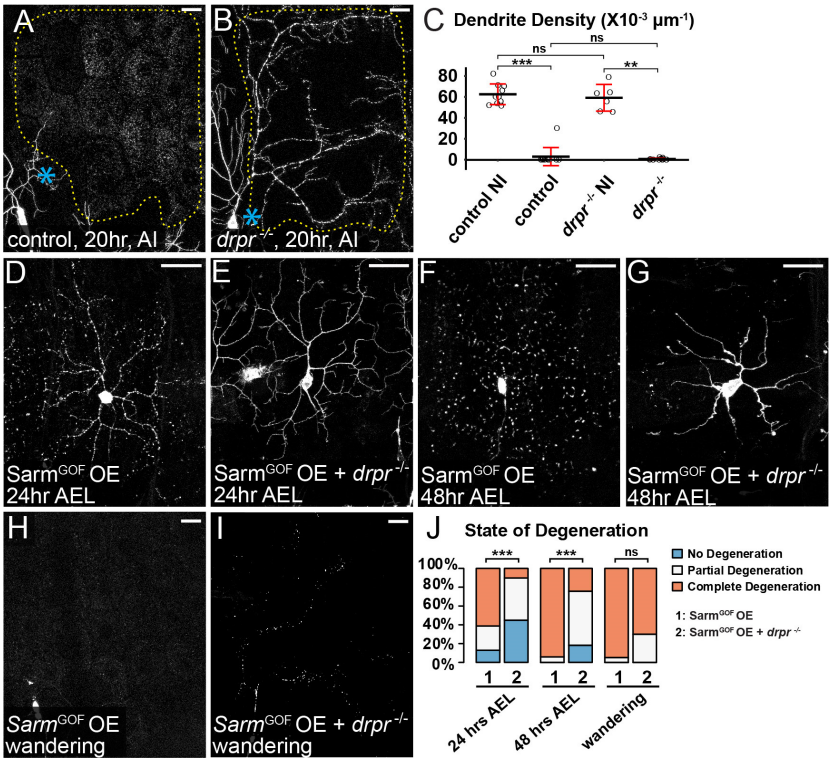

Figure 5: Injury and NAD$^+$ depletion cause phagocytosis-independent dendrite self-destruction

(A-B) Partial dendritic fields of ddaC neurons in control (A) and *drpr*$^{-/-}$ (B) animals 20 hrs AI. The dendrite debris lining up in the original dendritic pattern in (B) indicates dendrite fragmentation and the lack of epidermal engulfment. Blue asterisk, injury site. Yellow dots outline regions covered by injured dendrites.

(C) Quantification of dendrite density. n = number of neurons: control no-injury (NI) (n = 10, 10 animals); control AI (n = 12, 6 animals); *drpr*$^{-/-}$ NI (n = 6, 5 animals); *drpr*$^{-/-}$ AI (n = 13, 5 animals). Kruskal-Wallis (One-way ANOVA on ranks) and Dunn's test, p-values adjusted with the Benjamini-Hochberg method.

(D-G) ddaC neurons in *Sarm*^{GOF} OE 24 hrs after egg laying (AEL) (D), *Sarm*^{GOF} OE + *drpr*$^{-/-}$ 24 hrs AEL (E), *Sarm*^{GOF} OE 48 hrs AEL (F) and *Sarm*^{GOF} OE + *drpr*$^{-/-}$ 48 hrs AEL (G).

(H-I) Partial dendritic fields of *Sarm*^{GOF} OE (H) and *Sarm*^{GOF} OE + *drpr*$^{-/-}$ (I) ddaC neurons at the wandering stage.

(J) Quantification of dendrite degeneration showing percentages of neurons undergoing partial degeneration, complete degeneration, and no degeneration. n = number of neurons: *Sarm*^{GOF} OE 24 hrs AEL (n = 31, 7 animals); *Sarm*^{GOF} OE + *drpr*$^{-/-}$ 24 hrs AEL (n = 49, 17 animals); *Sarm*^{GOF} OE 48 hrs AEL (n = 17, 7 animals); *Sarm*^{GOF} OE + *drpr*$^{-/-}$ 48 hrs AEL (n = 33, 11 animals); *Sarm*^{GOF} OE wandering (n = 19, 14 animals); *Sarm*^{GOF} OE + *drpr*$^{-/-}$ wandering (n = 10, 6 animals). Freeman-Halton extension of Fisher's exact test.

In image panels above, neurons were labeled by *ppk-MApHS* (A and B) and *ppk>CD4-tdTom* (D-I). C4da-specific KO was induced by *ppk-Cas9*. For all quantifications, **p≤0.01, ***p≤0.001; n.s., not significant. Black bar, mean; red bar, SD. Scale bars, 25 µm.

236 program triggered by NAD^+ depletion is known to drive WD of cultured neurons in the absence
237 of phagocytes (Gerdts et al., 2015). To test the possibility that a further NAD^+ reduction beyond
238 the level that triggers PS exposure causes phagocytosis-independent dendrite self-destruction, we
239 tested the effect of overexpressing a gain-of-function Sarm ($Sarm^{GOF}$) in C4da neurons, because
240 $Sarm^{GOF}$ potently depletes NAD^+ and causes dominant neurodegeneration (Neukomm et al.,
241 2017). Indeed, $Sarm^{GOF}$ OE caused complete dendrite degeneration in most neurons as early as
242 24 hrs after egg laying (AEL) (Figures 5D and 5J), while *Nmnat* KO did not cause dendrite
243 degeneration until 88-91 hrs AEL. Supporting the role of engulfment in NAD^+ reduction-induced
244 dendrite degeneration, *drpr* LOF strongly suppressed dendrite degeneration of $Sarm^{GOF}$ OE
245 neurons at both 24 hrs AEL and 48 hrs AEL (Figures 5E, 5G, and 5J). However, *drpr* LOF failed
246 to prevent dendrite fragmentation of $Sarm^{GOF}$ OE neurons at wandering 3rd instar (Figures 5H-
247 5J), suggesting that NAD^+ depletion is able to cause phagocytosis-independent dendrite self-
248 destruction. These results together support the hypothesis that dendrite self-destruction induced
249 by NAD^+ depletion is responsible for the fragmentation of injured dendrites when phagocytosis
250 is suppressed.

251 **Axed promotes self-destruction of injured dendrites in parallel with PS-mediated**
252 **phagocytosis**

253 To understand how other components of the WD pathway regulate dendrite degeneration, we
254 examined LOF of *axed* and *peb*. Tissue-specific KO of *axed* in Or22a olfactory neurons, an
255 established axon-injury model (MacDonald et al., 2006), effectively blocked degeneration of
256 severed axons 7 days after antenna ablation (Figure S1A-S1D, and S1G), demonstrating the
257 effectiveness of the gRNAs. In C4da neurons, both KO and knockdown (KD) of *axed* also
258 efficiently blocked injury-induced axon degeneration (Figures S1H-S1K), consistent with the
259 role of Axed in WD. To test if Axed is involved in PS exposure-induced dendrite degeneration
260 resulting from *Nmnat* LOF, we knocked out both *Nmnat* and *axed* in da neurons. Unlike *Sarm*
261 KO, which fully rescued *Nmnat* KO-induced degeneration (Figures S1M, S1O, S1P, and S1Q),
262 *axed* KO did not affect dendrite degeneration caused by *Nmant* KO (Figures S1L, S1N, S1P, and
263 S1Q), suggesting that *axed* is not required for the PS exposure induced by NAD^+ reduction.

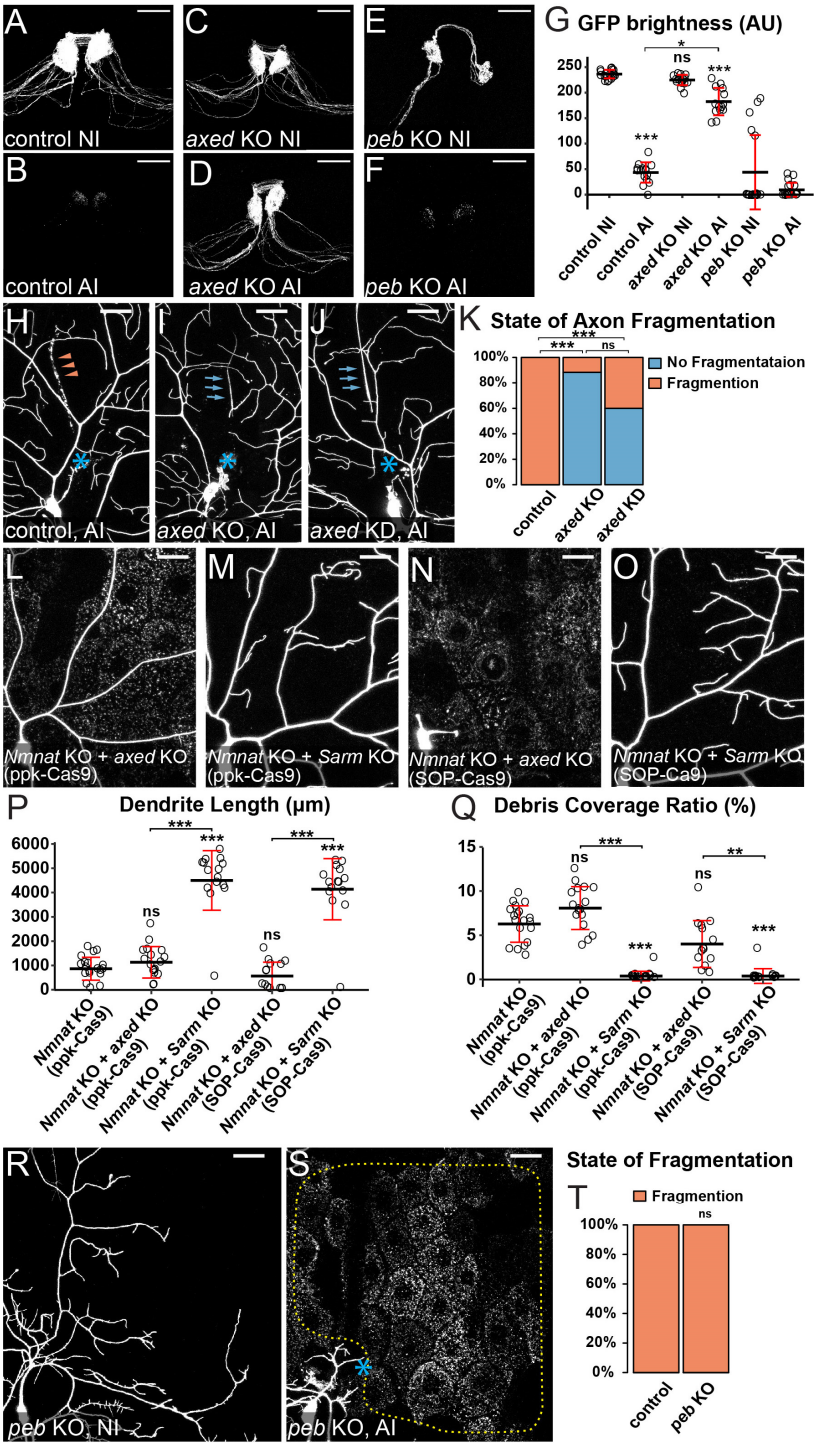

Figure S1: Axed is not involved in PS-mediated phagocytosis

(A-F) Axons of control NI (A), control 7 days AI (B), *axed* KO NI (C), *axed* KO 7 days AI (D), *peb* KO NI (E), and *peb* KO 7 days AI (F) Or22a neurons in 14-day-old adult brains. Or22a neurons were labeled by *Or22a>CD8-GFP* and KO was induced by *ey-Cas9*. Scale bars, 25 µm.

(G) Quantification of GFP brightness of Or22a glomeruli. n = number of brains: control NI 14 days (n = 19); control 7 days AI 14 days (n = 15); *axed* KO NI 14 days (n = 16); *axed* KO 7 days AI 14 days (n = 14); *peb* KO NI 14 days (n = 18); *peb* KO 7 days AI 14 days (n = 20). Kruskal-Wallis (One-way ANOVA on ranks) and Dunn's test, p-values adjusted with the Benjamini-Hochberg method. *p≤0.05, ***p<0.001, n.s., not significant. The significance level above each genotype is for comparison with the control. Statistical comparisons for *peb* KO glomeruli are not shown due to the variation within the group of *peb* KO NI 14 days. Black bar, mean; red bar, SD.

(H-J) Injured axons of wildtype 24 hrs AI (H), *axed* KO AI 24 hrs AI (I), and *axed* KD AI 24 hrs AI (J). Neurons were labeled by *ppk-MApHS*. Neuronal-specific KO was induced by *SOP-Cas9*, and neuronal-specific KD was driven by *21-7 Gal4*. Scale bars, 25 µm.

(K) Quantification of axon fragmentation showing percentages of neurons undergoing no fragmentation, and complete fragmentation of injured axons at 24 hrs AI. n = number of neurons: wildtype 24 hrs AI (n = 20, 12 animals); *axed* KO 24 hrs AI (n = 17, 9 animals); *axed* KD 24hrs AI (n = 20, 8 animals). Freeman-Halton extension of Fisher's exact test. For all quantifications, ***p≤0.001; n.s., not significant.

(L-O) Partial dendritic fields of *Nmnat* KO + *axed* KO (L and N) and *Nmnat* KO + *Sarm* KO (M and O) ddaC C4da neurons. Neurons were labeled by *ppk>CD4-tdTom* (L-O). The C4da-specific KO was induced by *ppk-Cas9* (L-M) or by *SOP-Cas9* (N-O). Scale bars, 25 µm.

(legends continued on the next page)

264

(continued) (P) Quantification of dendrite length. n = number of neurons: *Nmnat* KO (*ppk-Cas9*) (n = 19, 10 animals); *Nmnat* KO + *axed* KO (*ppk-Cas9*) (n = 17, 9 animals); *Nmnat* KO + *Sarm* KO (*ppk-Cas9*) (n = 16, 8 animals); *Nmnat* KO + *axed* KO (*SOP-Cas9*) (n = 14, 7 animals); *Nmnat* KO + *Sarm* KO (*SOP-Cas9*) (n = 15, 8 animals). One-way ANOVA and Tukey's test.

(Q) Quantification of debris coverage ratio, which is the percentage of debris area normalized by dendrite area ratio. Number of neurons: same as in (P). Kruskal-Wallis (One-way ANOVA on ranks) and Dunn's test, p-values adjusted with the Benjamini-Hochberg method.

For all quantifications, **p≤0.01; ***p≤0.001; n.s., not significant. The significance level above each genotype is for comparison with the control. Black bar, mean; red bar, SD.

(R-S) Partial dendritic fields of *peb* KO NI (R) and *peb* KO 24 hrs AI (S) ddaC neurons. Yellow dots outline regions covered by injured dendrites in (S). Neurons were labeled by *ppk>CD4-tdTom* and neuronal-specific KO was induced by *SOP-Cas9*. Scale bars, 25 µm.

(T) Quantification of dendrite fragmentation showing percentages of neurons undergoing complete fragmentation of injured dendrites at 24 hrs AI. n = number of neurons: wildtype 24 hrs AI (n = 21, 12 animals); *peb* KO 24 hrs AI (n = 12, 7 animals). Freeman-Halton extension of Fisher's exact test. For all quantifications, n.s., not significant.

265 We next asked if Axed is involved in injury-induced dendrite degeneration. Injured
266 dendrites of wildtype neurons completely fragmented by 10 hrs AI (Figures 6A and 6E). *axed*
267 KO in neurons resulted in incomplete and no fragmentation of injured dendrites only in small
268 fractions (25% and 8%, respectively) of neurons (Figures 6B and 6E), suggesting that *axed* is not
269 absolutely required for the degeneration of injured dendrites. We next asked if Axed specifically
270 contributes to self-destruction of injured dendrites. Because PS-induced phagocytosis may be
271 sufficient to break down injured dendrites by 10 hrs AI, thereby masking dendrite protection by
272 *axed* KO, we examined the effect of *axed* KO in *drpr* mutant. *drpr* LOF alone caused incomplete
273 and no dendrite fragmentation in 36% and 23% injured neurons, respectively (Figures 6C and
274 6E), consistent with the idea that phagocytosis contributes significantly to dendrite breakdown at
275 this stage. In comparison, *axed* KO in *drpr* mutant strongly blocked dendrite degeneration at 10
276 hrs AI, with 56% incomplete fragmentation and 36% no fragmentation (Figures 6D and 6E),
277 suggesting that *axed* KO and *drpr* LOF have an additive effect in dendrite protection.
278 Surprisingly, this combined protection was significantly weakened by 24 hrs AI, with only 47%
279 incomplete fragmentation and 5% no fragmentation (Figures 6F-6J). These data suggest that
280 Axed promotes dendrite self-destruction in parallel with PS-induced phagocytosis; however,
281 other factors can also cause self-destruction in the absence of Axed.

282 In contrast to *axed*, *peb* KO in C4da neurons did not block dendrite fragmentation after
283 injury but altered dendrite morphology (Figures S1R-S1T). Unexpectedly, knocking out *peb*
284 from precursors of Or22a neurons caused loss of some or all of Or22a axons in uninjured adult
285 brains (Figure S1G), suggesting that *peb* plays a role in Or22a development or axon patterning.

The remaining axons of *peb* KO neurons did not show defects in axon degeneration after injury (Figures S1E-S1G). These results suggest that Peb may be a neuronal type-specific modulator of the WD pathway and is not required for dendrite degeneration of da neurons.

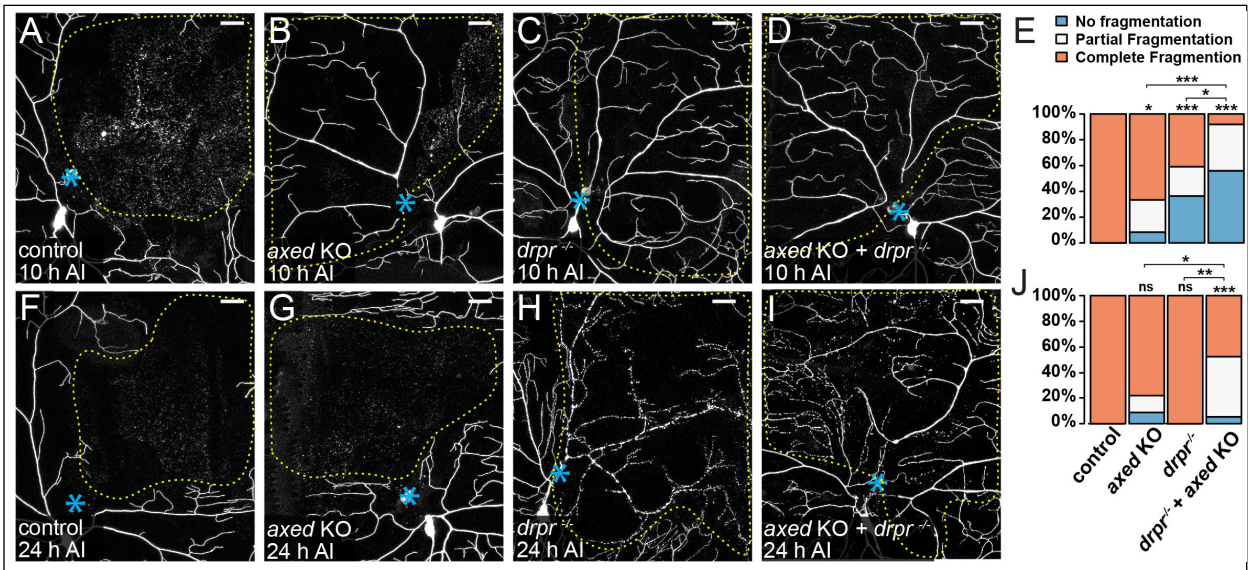

Figure 6: Axed drives dendrite self-destruction in parallel with PS-mediated phagocytosis

(A-D) Partial dendritic fields of wildtype (A), *axed* KO (B), *drpr*$^{-/-}$ (C), and *axed* KO + *drpr*$^{-/-}$ (D) ddaC neurons 10 hrs AI. (B) shows partial fragmentation; (C) and (D) show no fragmentation.

(E) Quantification of dendrite fragmentation showing percentages of neurons undergoing no fragmentation, partial fragmentation, and complete fragmentation of injured dendrites at 10 hrs AI. n = number of neurons: wildtype (n=18, 9 animals); *axed* KO (n = 24, 10 animals); *drpr*$^{-/-}$ (n = 22, 11 animals); *axed* KO + *drpr*$^{-/-}$ (n = 25, 11 animals). Freeman-Halton extension of Fisher's exact test.

(F-I) Partial dendritic fields of wildtype (F), *axed* KO (G), *drpr*$^{-/-}$ (H), and *axed* KO + *drpr*$^{-/-}$ (I) ddaC neurons 24 hrs AI. (I) shows partial fragmentation. In all image panels, blue asterisks indicate injury sites; yellow dots outline regions covered by injured dendrites. Neurons were labeled by *ppk>CD4-tdTom* (A, B, F and G) and *ppk-CD4-tdTom* (C, D, H, and I). Neuronal-specific KO was induced by *SOP-Cas9* (B, D, G, and I). Scale bars, 25 µm.

(J) Quantification of dendrite fragmentation showing percentages of neurons undergoing no fragmentation, partial fragmentation, and complete fragmentation of injured dendrites at 24 hrs AI. n = number of neurons: wildtype (n=21, 12 animals); *axed* KO (n = 23, 10 animals); *drpr*$^{-/-}$ (n = 12, 5 animals); *axed* KO + *drpr*$^{-/-}$ (n = 19, 8 animals). Freeman-Halton extension of Fisher's exact test. For all quantifications, *p≤0.05, **p≤0.01, ***p≤0.001; n.s., not significant. The significance level above each genotype is for comparison with the wildtype.

Injured dendrites undergo severe membrane rupture during dendrite fragmentation

To further understand how injury induces dendrite degeneration, we investigated the extent of membrane rupture during dendrite breakdown using a split GFP-based assay. In this membrane rupture assay (Figure 7A), neurons express myristoylated tdTom-GFP(1-10) and the fat body secretes GFP(11)x7 into the hemolymph. GFP(11)x7 will bind myr-tdTom-GFP(1-10) and reconstitute fluorescent GFP only when the dendrite membrane is ruptured to allow diffusion of GFP(11)x7 into the cytoplasm of neurons. While reconstituted GFP was not detected in uninjured wildtype dendrites (Figure S2A) or degenerating dendrites of *Nmnat* KO neurons

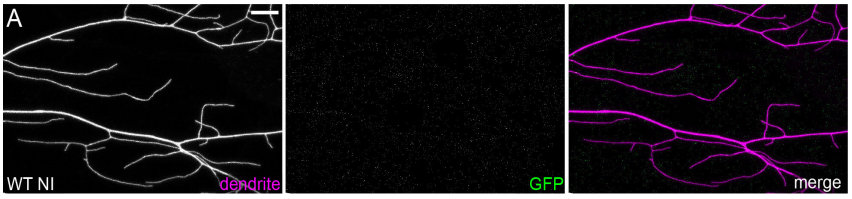

Figure S2: Membrane of uninjured dendrites does not rupture.

(A) Uninjured wildtype dendrites lacking reconstituted GFP in the membrane rupture assay. Scale bar, 25 µm.

(Figures 7B, open arrowheads, and 7D-7E), it was observed in severed wildtype dendrites that were undergoing blebbing and fragmentation (Figures 7C, arrowheads, and 7E), as well as on membrane pieces shed from injured dendrites (Figure 7C, arrows, and 7D). In time-lapse movies, GFP signals were visible at low levels in injured branches soon after laser ablation, likely due to GFP(11)$_{x7}$ entry through the injury site. The signals were kept at constantly low levels until injured dendrites fragmented, when GFP signals rapidly increased in large dendrite particles (Video 3). These results suggest that injured dendrites undergo severe membrane rupture during fragmentation. In contrast, *Nmnat* KO neurons experience much milder disruptions of membrane

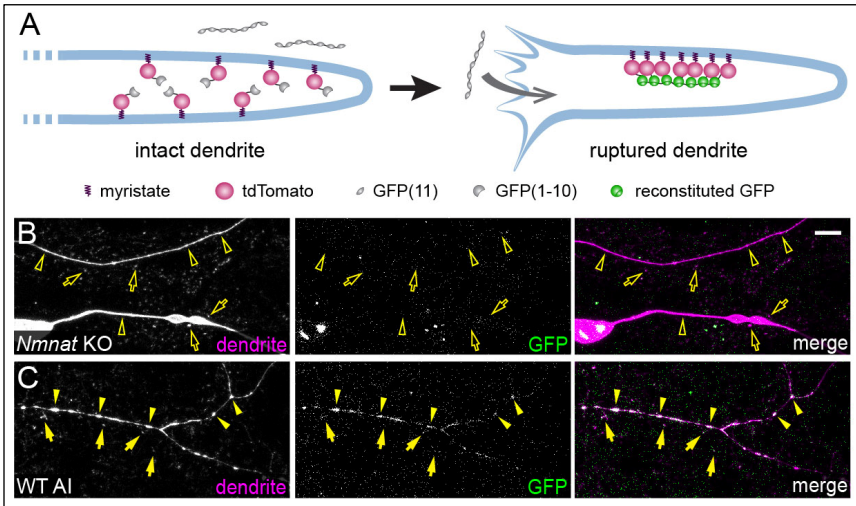

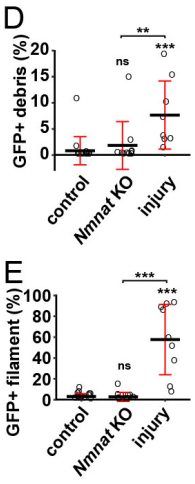

Figure 7. Injured dendrites undergo severe membrane rupture during dendrite fragmentation

(A) A diagram for the membrane rupture assay. Extracellular GFP(11)$_{x7}$ is separated from intracellular myr-tdTom-GFP(1-10) attached to the inner membrane of dendrites. Fluorescent GFP is reconstituted only when the dendrite membrane is ruptured to allow diffusion of GFP(11)$_{x7}$ into the cytoplasm of neurons.

(B) *Nmnat* KO dendrites (open arrowheads) and debris (open arrows) lacking reconstituted GFP in the membrane rupture assay. Scale bar, 25 µm.

(C) Reconstituted GFP labeling of injured wildtype dendrites (arrowheads) and debris (arrows) in the membrane rupture assay. Scale bar, 25 µm. See also Video 3.

(D) Quantification of GFP-positive debris, showing the percentage of GFP-positive debris area in tdTom-positive debris area. Number of ROIs: wildtype NI (n= 15, 7 animals); *Nmnat* KO NI (n= 10, 6 animals) wildtype 6 hrs AI (n= 10, 4 animals). Kruskal-Wallis (One-way ANOVA on ranks) and Dunn's test, p-values adjusted with the Benjamini-Hochberg method.

(E) Quantification of GFP-positive filament, showing the percentage of GFP-positive filament area in tdTom-positive filament area. Number of ROIs: same as in (D). Kruskal-Wallis (One-way ANOVA on ranks) and Dunn's test, p-values adjusted with the Benjamini-Hochberg method.

For all quantifications, **p≤0.01; ***p≤0.001; n.s., not significant. The significance level above each genotype is for comparison with the control. Black bar, mean; red bar, SD.

305 integrity, even though they are losing membranes due to the attack of epidermal cells, probably
306 because their dynamically growing branches are efficient in repairing membrane damages.

307 **Injured dendrites exhibit calcium flashing that is suppressed by Wld^{S} and *axed* loss**

308 The observed membrane rupture of injured dendrites is consistent with phagocytic attacks of
309 epidermal cells on PS-exposing dendrites (Figure 7C). To understand potential signaling events
310 that may lead to dendritic PS exposure and membrane rupture, we examined calcium dynamics
311 in injured dendrites using long-term time-lapse imaging (Ji and Han, 2020; Poe et al., 2017),
312 because calcium influx is essential for and correlates with degeneration of damaged axons in
313 neuronal culture and *in vivo* (George et al., 1995; Vargas et al., 2015; Williams et al., 2014). A
314 previous study in zebrafish identified an initial calcium influx at the time of axon severing and a
315 second calcium wave that coincides with axon fragmentation (Vargas et al., 2015). We recorded
316 calcium dynamics using a membrane-tethered GCaMP6s (myr-GCaMP6s) (Akbergenova et al.,
317 2018), which detected only occasional local rise of calcium in dendrites of wildtype (Video 4)
318 and *Nmnat* KO neurons (Video 5). In the injury model, we observed an initial calcium rise
319 immediately after laser injury in both detached dendrites and the rest of the neurons (Figure 8A,
320 2s AI). Interestingly, soon after calcium dropped to the baseline level, severed dendrites but not
321 those connected to the cell body entered a phase of continuous calcium flashes that lasted 1-5
322 hours (Figures 8A at 1h AI, 8D, and Video 6). Afterward, severed dendrites stayed relatively
323 quiescent for 1-3 hrs before calcium surged again at the time of dendrite blebbing and
324 fragmentation (Figures 8A at 6h AI, 8D, and Video 6). All severed dendrites but not those still
325 attached to cell bodies showed flashing, quiescence, and surge phases after injury, even though
326 the exact timing and duration of each phase varied from dendrite to dendrite (Figures S3A and
327 S3D).

328 It was reported that nanoscale ruptures of the axonal plasma membrane are responsible
329 for extracellular calcium influx in neuroinflammatory lesions (Witte et al., 2019) and after spinal
330 cord contusion (Williams et al., 2014). To determine whether the last calcium rise that coincides
331 with dendrite degeneration could be a result of phagocytosis-induced membrane breakage, we
332 imaged both calcium dynamics and PS exposure of injured dendrites using the PS sensor
333 Annexin V-mCardinal (AV-mCard) (Sapar et al., 2018). AV-mCard labeling of dendrites
334 appeared slightly ahead of the final calcium surge (Figures 8B and 8C, Video 7). Considering

335 that Annexin V-binding to PS and accumulation on dendrite surface are likely slower than
336 calcium activation of GCaMP6s, our data support the idea that PS-mediated phagocytosis causes
337 dendrite membrane rupture and the final calcium surge.

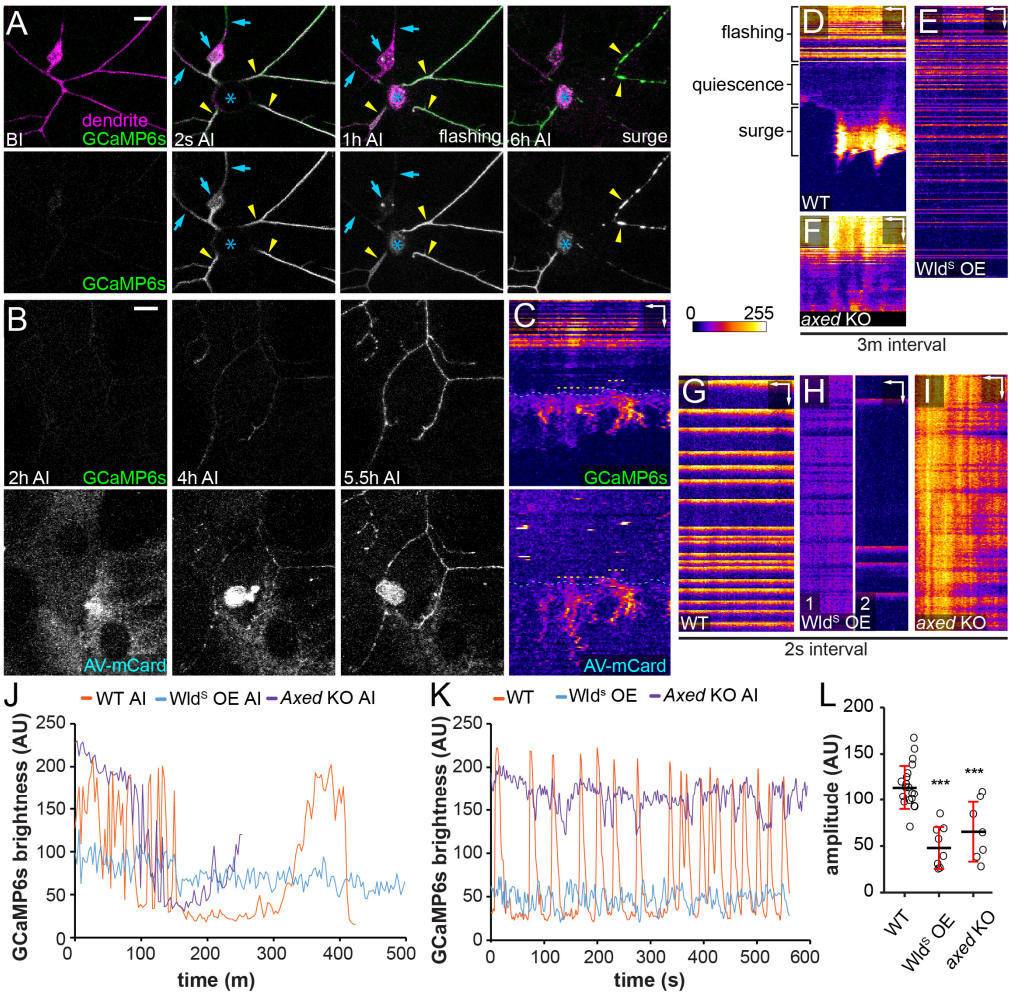

Figure 8: Calcium flashing precedes PS exposure and fragmentation of injured dendrites

(A) A ddaC neuron in a 3rd instar larva expressing myr-GCaMP6s before (BI) and after (2s AI, 1h AI, and 6h AI) laser injury. Blue arrows, uninjured dendrites or cell body; yellow arrowheads, injured dendrites; blue asterisk, injury site. Scale bar, 10 µm. See also Video 6.

(B) Labeling of injured ddaC dendrites expressing GCaMP6s by AV-mCard after (2 h, 4 h, and 5.5 h) injury. Scale bar, 10 µm. See also Video 7.

(C) Kymograph of GCaMP6s signal and AV-mCard binding on an injured dendrite shown in B. Yellow dotted lines, timing of AV-mCard binding; blue dotted lines, timing of the final calcium surge. Scale bars, 3 µm horizontal, 40 min vertical.

(D-F) Kymograph of GCaMP6s signal in wildtype (D), Wld^S-overexpressing (E), and *axed* KO (F) dendrites after injury with 3-min interval. Scale bar, 5 µm horizontal, 60 min vertical. See also Videos 6, 8 and 12.

(G-I) Kymograph of GCaMP6s signal in wildtype (G), Wld^S-overexpressing (H), and *axed* KO (I) dendrites after injury with 2-s interval. See also Videos 9-11 and 13. Scale bars, 5 µm horizontal, 45 sec vertical.

(J) Plot of GCaMP6s brightness in injured dendrites in (D), (E), and (F) over time with 3-m interval. Measurements in injured dendrites start from 0.5-1 hr AI.

(K) Plot of GCaMP6s brightness in injured dendrite in (G), (H), and (I) over time with 2-s interval. Measurements start from 0.5-1 hr AI.

(L) Quantification of average flashing amplitude (GCaMP6s brightness difference between maximum peak and neighboring minimum peak) captured in 2 s-interval time-lapse images. n=number of dendrite arbors: wildtype 0.5-1.5 hrs AI (n= 19, 5 animals); Wld^S-overexpressing 2 hrs AI (n=8, 4 animals); *axed* KO 0.5-1 hrs AI (n=7, 3 animals). One-way ANOVA and Tukey's test. For all quantifications, ***$p \leq 0.001$; n.s., not significant. The significance level above each genotype is for comparison with the control. Black bar, mean; red bar, SD.

338 Because the unique pattern of calcium flashing is absent in uninjured dendrites and
339 *Nmnat* KO neurons, we suspected that it may play an active role in promoting degeneration of
340 injured dendrites. If so, factors that can block dendrite degeneration may also alter the calcium
341 flashing. Indeed, Wld^S OE dramatically reduced calcium fluctuations in injured dendrites and
342 eliminated the quiescent and surge phases for the entire duration of our time-lapse imaging (13
343 hrs) (Figures 8E, 8J, S3B, and Video 8). In addition, using time-lapse imaging at a higher
344 temporal resolution (2 s/frame), we found that wildtype injured dendrites displayed calcium
345 flashes at a frequency of 0.4-3/min (Figures 8G and 8K, and Video 9) while injured dendrites of

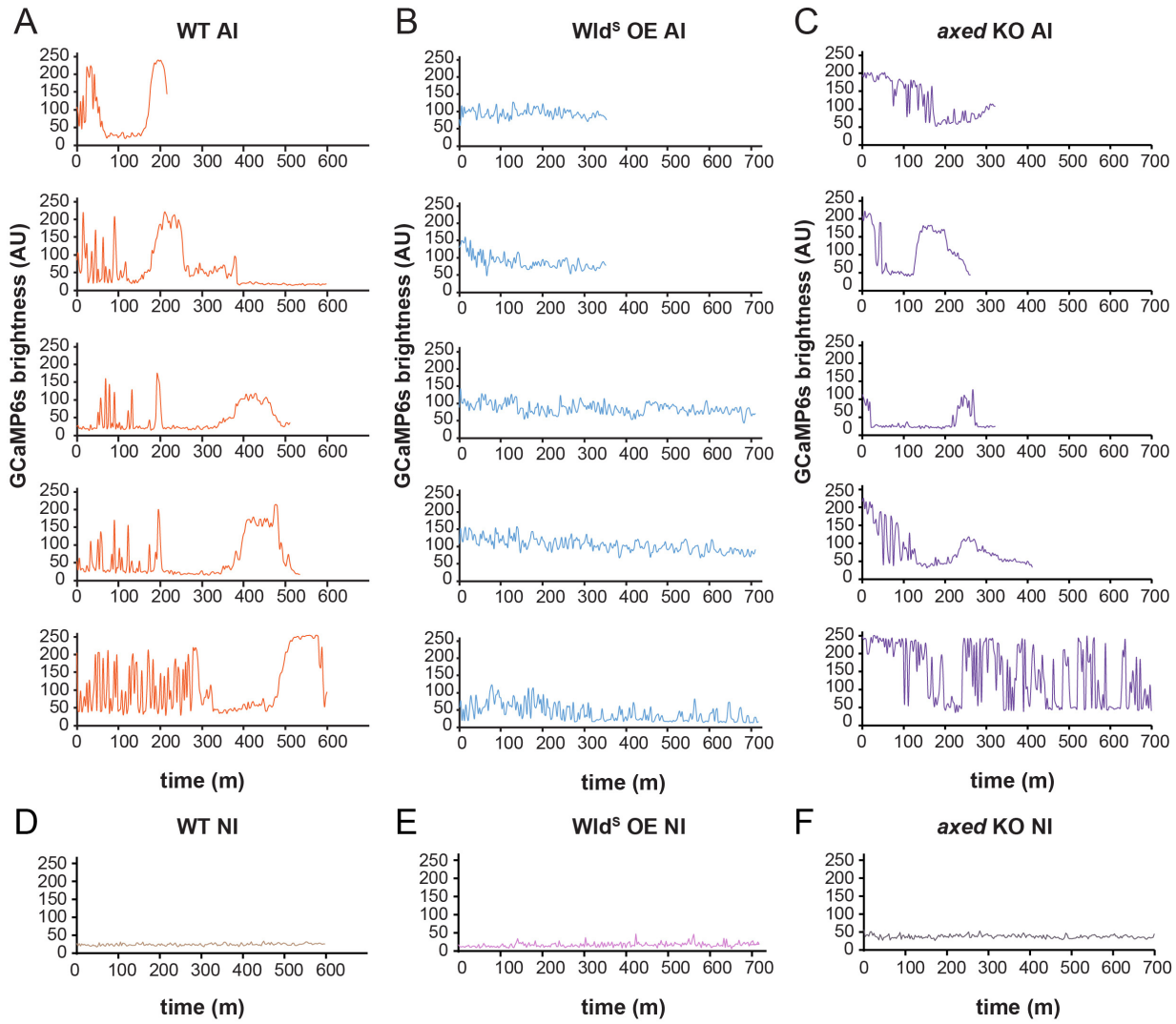

Figure S3: Wld^S overexpression and loss of *axed* changed calcium flashes in injured dendrites.

(A-C) Representative plots of GCaMP6s brightness in injured dendrites of wildtype (A), Wld^S-overexpressing (B), and *axed* KO (C) neurons over time with 3-min interval.

(D-F) Representative plots of GCaMP6s brightness in uninjured dendrites of wildtype (A), Wld^S-overexpressing (B), and *axed* KO (C) neurons over time with 3-min interval.

346 Wld^S OE neurons either maintained a much milder calcium fluctuation or exhibited irregular and
347 infrequent calcium flashes (Figures 8H and 8K-8L; Videos 10 and 11). In contrast, the majority
348 of severed dendrites of *axed* KO neurons (6/9) maintained constant and high calcium levels
349 before the quiescence and surge phases (Figures 8F, 8J, S3C, and Video 12), which was further
350 confirmed by time-lapse imaging at the high temporal resolution (Figures 8I, 8K, 8L, S3C, and
351 Video 13). Overall, injured dendrites of Wld^S OE and *axed* KO neurons showed much smaller
352 average amplitudes of calcium fluctuations compared to the wildtype control (Figure 8L).
353 Because Wld^S OE and *axed* KO did not alter calcium dynamics in uninjured dendrites (Figures
354 S3E and S3F), these data suggest that these manipulations specifically modify calcium flashing
355 patterns in injured dendrites, consistent with the idea that calcium flashes may promote
356 degeneration of injured dendrites.

357 **DISCUSSION**

358 In this study, we investigate the mechanism of dendrite degenerations caused by genetic NAD^+
359 disruptions and injury in the *Drosophila* PNS. Although neurite phagocytosis has been observed
360 after neuronal injury both *in vivo* and *in vitro* (Han et al., 2014; MacDonald et al., 2006;
361 Nomura-Komoike et al., 2020; Sapar et al., 2018), WD is generally thought as a result of neurite
362 self-destruction triggered by NAD^+ depletion (Babetto et al., 2013; Gerdts et al., 2015; Gerdts et
363 al., 2016; Neukomm et al., 2017). However, our results using the engulfment-deficient *drpr*
364 mutant strongly suggest that PS-mediated phagocytosis is the main driving force for NAD^+
365 reduction-related dendrite degeneration *in vivo*. It is solely responsible for dendrite degeneration
366 of *Nmnat* KO neurons and greatly accelerates the degeneration of $Sarm^{GOF}$ OE neurons. In
367 injury, phagocytosis is responsible for at least half of the dendrite fragmentation by 10 hrs AI
368 and may contribute more to dendrite breakdown than self-destruction at earlier stages.

369 Supporting this idea, ectopic PS exposure on injured dendrites is sufficient to revert the blockage
370 of dendrite fragmentation by Wld^S OE or *Sarm* KO, even though ectopically induced PS
371 exposure is much lower than natural PS exposure on injured dendrites (Sapar et al., 2018). Our
372 time-lapse analyses of PS exposure, the final calcium surge, and dendrite rupture also support
373 that PS-mediated phagocytosis breaks down injury dendrites at the time of dendrite
374 fragmentation. Therefore, at least in the context of dendrite injury, phagocytosis is the major

375 factor driving degeneration while self-
376 destruction acts as a secondary
377 mechanism to ensure complete
378 fragmentation.

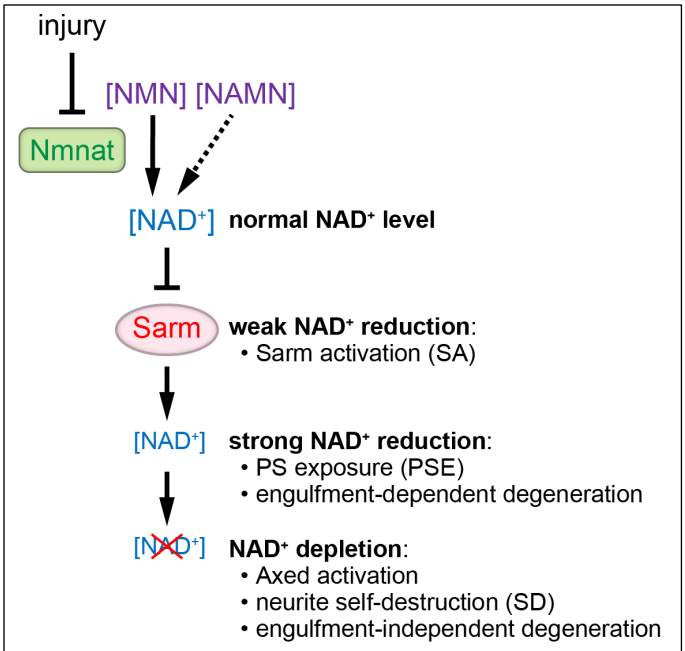

Figure 9. Three levels of NAD$^+$ reduction elicit distinct responses in dendrites.
See Discussion for details.

379 NAD$^+$ reduction is known to be
380 essential for neuronal PS exposure and
381 neurite self-destruction during WD
382 (Gerdts et al., 2015; Sapar et al., 2018;
383 Shacham-Silverberg et al., 2018). How
384 does the same signaling input coordinate
385 the two different events? Our results show
386 that NAD$^+$ disruption controls PS
387 exposure and neurite self-destruction in
388 separate steps of WD. In the existing
389 model, Sarm activation is believed to cause catastrophic NAD$^+$ depletion that is sufficient to
390 initiate neurite self-destruction (Gerdts et al., 2015; Sasaki et al., 2016). However, we found that
391 downstream of Sarm activation and before the initiation of self-destruction, neurites first expose
392 PS to engage in phagocytosis-mediated non-autonomous degeneration. Therefore, in our revised
393 model, dendrites respond to at least three distinct, increasingly severe levels of NAD$^+$ reduction
394 by eliciting different molecular events (Figure 9). Between the NAD$^+$ level required for Sarm
395 activation (SA level) and the level that initiates self-destruction (SD level), Sarm activity lowers
396 NAD$^+$ to a level that causes neurons to expose PS on their surface (which we call the PSE level).
397 This PS exposure is sufficient to cause phagocytosis-mediated dendrite degeneration, which can
398 be completely prevented by blocking engulfment activity of phagocytes. However, below the SD
399 level, neurites spontaneously fragment even in the absence of phagocytosis.

400 Our results also suggest a direct correlation between the kinetics of NAD$^+$ reduction and
401 the severity of neurite degeneration. *Nmnat* KO is expected to cause slow NAD$^+$ reduction, due
402 to gene perdurance and the time required for natural NAD$^+$ turnover, and correspondingly causes
403 engulfment-dependent dendrite degeneration only in late 3rd instar larvae. In contrast, Sarm^{GOF}
404 OE should lead to a more rapid NAD$^+$ depletion and in fact causes engulfment-dependent
405 dendrite degeneration as early as the 1st instar and dendrite self-destruction by the 3rd instar.

406 Injury is known to cause even more rapid NAD^+ reduction in axons (Wang et al., 2005) and is
407 correlated with the fastest dendrite degeneration – initiation at around 4 hrs AI and completion
408 usually by 10 hrs AI.

409 How does NAD^+ reduction cause PS exposure? A direct consequence of NAD^+ loss is the
410 decline of neurite ATP levels due to the requirement of NAD^+ in glycolysis and oxidative
411 phosphorylation (Shacham-Silverberg et al., 2018; Wang et al., 2005). Consistent with ATP
412 reduction playing a role in inducing PS exposure, suppressing mitochondria ATP synthesis in
413 DRG culture caused gradual axonal PS exposure (Shacham-Silverberg et al., 2018). However,
414 how ATP reduction may induce PS exposure remain elusive. Although the maintenance of
415 membrane PS asymmetry by flippases requires ATP, flippase KO in C4da neurons causes a
416 much milder PS exposure than injury (Sapar et al., 2018), suggesting that mechanisms other than
417 flippase inhibition must be contributing to the rapid PS exposure seen after injury. Identifying
418 the PS transporters responsible for PS exposure on injured neurites will be a key step for
419 revealing the mechanisms of NAD^+ regulation of PS exposure.

420 Genetic analyses in *Drosophila* identified Axed as a key switch of WD, whose activity is
421 absolutely required for axon degeneration caused by injury and genetic depletion of NAD^+
422 (Neukomm et al., 2017). How does Axed regulate neurite degeneration? Our data suggest that
423 Axed is not required for PS-mediated phagocytosis but contributes to self-destruction of injured
424 dendrites, placing its activation below the SD level of NAD^+ (Figure 9). Surprisingly, Axed
425 seems to play a minor role in dendrite degeneration, as its LOF only slowed down but did not
426 block self-destruction, indicating the existence of other factors that promote self-destruction of
427 injured dendrites. Importantly, these results suggest that dendrites and axons may rely on
428 different mechanisms of self-destruction.

429 By exploring the different mechanisms employed in *Nmnat* KO- and injury-induced
430 dendrite degenerations, we discovered dynamic calcium activities only present in injured
431 dendrites, including an unreported calcium flashing pattern prior to any obvious degenerative
432 event and a final calcium surge that coincides with dendrite fragmentation. Calcium surge at the
433 time of neurite fragmentation is a shared feature between injured axons of zebrafish (Vargas et
434 al., 2015) and injured dendrites of *Drosophila* da neurons. Although calcium influx is required
435 for WD (George et al., 1995) and may activate calcium-dependent lipid scramblases (Suzuki et

436 al., 2010), our time-lapse analyses suggest that the final calcium surge is more likely a result of
437 phagocytosis-induced membrane rupture rather than the cause of fragmentation. In comparison,
438 the calcium flashing soon after the injury is unique to dendrites and may play an active role in
439 dendrite degeneration in ways similar to the compartmentalized calcium flashing that occurs
440 during developmental pruning of C4da neurons (Kanamori et al., 2013). Consistent with this
441 possibility, the calcium flashing is suppressed by Wld^S OE and *axed* KO. Interestingly, these two
442 manipulations block the calcium flashing in opposite ways, with Wld^S OE dampening the
443 calcium level and *axed* KO keeping the calcium level high. This distinction may be a useful clue
444 for understanding the regulation of PS exposure and self-destruction. For example, it is possible
445 that elevated calcium levels prepare dendrites for PS exposure and drastic changes of calcium
446 levels promote dendrite self-destruction.

447 Lastly, as impairment of NAD^+ metabolism is a general feature of neurodegenerative
448 disorders including Leber congenital amaurosis (LCA), Alzheimer's disease, Parkinson's
449 disease, and retinal degenerations (Ali et al., 2013; Canto et al., 2015; Fang et al., 2017; Lin et
450 al., 2016; Verdin, 2015), phagocytosis may play important roles in the pathogenesis of these
451 diseases through dysregulated neuronal PS exposure.

452 **METHODS**

453 **Fly strains**

454 The details of fly strains used in this study are listed in the key reagent table. For labeling of
455 C4da neurons, we used *ppk-CD4-tdTom*, *ppk-MApHS*, and *ppk-Gal4 UAS-CD4-tdTom*. For
456 labeling PS exposure on dendrites, we used *dcg-Gal4 UAS-GFP-LactC1C2*, *R16A03-LexA*
457 *LexAop-GFP-LactC1C2*, and *dcg-Gal4 UAS-AnnexinV-mCard*. To label Or22a axons, we used
458 *Or22a-Gal4 UAS-mCD8-GFP*. To visualize dendrite rupture, we used *dcg-Gal4 UAS-*
459 *sGFP(11)x7* together with *ppk-LexA LexAop-myr-tdTom-GFP(1-10)*. To visualize calcium
460 activities in C4da dendrites, we used *ppk-LexA LexAop-myr-GCaMP6s.*

461 **Molecular cloning and transgenic flies**

462 *ey-Cas9*: Three tandem copies of a 211bp *ey* enhancer (corresponding to nucleotides 2577-2787
463 in GenBank accession number AJ131630) was inserted into XhoI/SalI sites of pENTR11
464 (Thermo Fisher Scientific). The resulting entry vector was combined with a Cas9 destination

465 vector which is similar to pDEST-APIC-Cas9 (Addgene 121657) but does not contain Inr, MTE,
466 and DPE in the Hsp70 core promoter (Poe et al., 2019) to generate the pAPIC-ey-Cas9
467 expression vector through a Gateway LR reaction.

468 *LexAop-myr-tdTom-GFP(1-10)*: pAPLO-CD4-tdTom (Poe et al., 2017) was digested by
469 BglII/AscI, blunted, and religated to remove an XbaI site before 13xLexAop2. The resulting
470 construct is called pAPLOm-CD4-tdTom. An myr-GFP fragment was isolated from pJFRC176-
471 10XUAS-rox-dSTOP-rox-myr-GFP (Addgene 32147) by XhoI/XbaI digestion and ligated to
472 XhoI/XbaI sites of pAPLOm-CD4-tdTom to make pAPLO-myr-GFP. pAPLO-myr-GFP was
473 then digested by BamHI/XbaI and subsequently assembled with a tdTom PCR fragment and a
474 GFP(1-10) gBlock fragment (synthesized by IDT) through NEBuilder DNA Assembly to
475 generate pAPLO-myr-tdTom-GFP1-10.

476 *UAS-sGFP(11)x7*: A DNA fragment containing GFP(11)x7 was PCR amplified from a gBlock
477 DNA fragment and cloned into Nhe/XbaI sites of pIHEU-sfGFP-LactC1C2 using NEBuilder
478 DNA Assembly. The resulting construct pIHEU-sGFP11x7 inherits the signal peptide sequence
479 from pIHEU-sfGFP-LactC1C2 but removes the sfGFP-LactC1C2 coding sequence.

480 *LexAop-WldS*: The WldS coding sequence was PCR amplified from UAS-WldS genomic DNA
481 and cloned into XhoI/XbaI sites of pAPLOm-CD4-tdTom via restriction cloning to make
482 pAPLO-WldS.

483 *UAS-ATP8A*: A fragment encoding a FLAG tag and the ER exit signal of Kir2.1 (Han et al.,
484 2011) was cloned into the EcoRI and XbaI sites of pACU (Han et al., 2011) by ligating with
485 annealed oligos. The ATP8A coding region that is shared by all isoforms was amplified by PCR
486 from cDNA clone GH28327 (AA26 to AA1091, BDGP) and inserted into an NheI site before the
487 FLAG tag.

488 *gRNA expression vectors*: For *Nmnat*, *Sarm*, and *axed*, gRNAs were cloned into pAC-U63-
489 tgRNA-Rev as described (Poe et al., 2019). The first tRNA spacer in each final construct is
490 $tRNA^{Gly}$ but the remaining tRNA spacers are $tRNA^{Gln}$ (Koreman et al., 2021). *gRNA-peb* was
491 constructed in pAC-U63-QtgRNA2.1-BR. The gRNA target sequences are listed in the table
492 below.

Gene	**Target sequence 1**	**Target sequence 2**

Sarm	GCATCTGTTCAAACACTCCG	CGATTCCAATATCAGCCCGG
Nmnat	GGAACCCACAGAGTGGTAGG	TAAGAGCCGCCGAATCAACG
axed	GTCGGTACTCGAGCGGAGCG	TGGACCCGATGGCCATCACG
peb	ATTTCGTCTGAATCGCTCGG	ACGCATGTGACGCACCAGGG

The above constructs were injected by Rainbow Transgenic Flies to transform flies through φC31 integrase-mediated integration into attP docker sites. The sequences of constructs will be provided upon request.

CRISPR-TRiM

The efficiency of transgenic gRNA lines was validated by the Cas9-LEThAL assay (Poe et al., 2019). Homozygous males of each gRNA line were crossed to *Act-Cas9 w lig4* homozygous females. *gRNA-Nmnat* crosses caused lethality of all progeny at the 2nd instar larval stage; *gRNA-Sarm* crosses yielded viable female progeny and male lethality between 3rd instar larvae to prepupae; *gRNA-axed* crosses caused lethality at the embryonic stage for all progeny; *gRNA-peb* crosses caused lethality from embryonic stage to the 2nd instar for all progeny. These results suggest that all gRNAs are efficient.

C4da-specific gene knockout was carried out using *ppk-Cas9* (Poe et al., 2019). Tissue-specific knockout in da neuron precursor cells were carried out with *SOP-Cas9* (Poe et al., 2019). Gene knockout in the precursor cells of Or22a ORNs was carried out using *ey-Cas9* (this study).

Live imaging

Animals were reared at 25°C in density-controlled vials (60-100 embryos/vial) on standard yeast-glucose medium (doi:10.1101/pdb.rec10907). Larvae at 125 hours AEL (wandering stage) or stages specified were mounted in 100% glycerol under coverslips with vacuum grease spacer and imaged using a Leica SP8 microscope equipped with a 40X NA1.30 oil objective. Larvae were lightly anesthetized with isoflurane before mounting. For consistency, we imaged dorsal ddaC neurons from A1-A3 segments (2-3 neurons per animal) on one side of the larvae. Unless stated otherwise, confocal images shown in all figures are maximum intensity projections of z

516 stacks encompassing the epidermal layer and the sensory neurons beneath, which are typically 8–
517 10 μm for 3rd instar larvae.

518 *Injury assay*

519 Injury assay at the larval stage was done as described previously (Sapar et al., 2018). Briefly,
520 larvae at 90 hr AEL were lightly anesthetized with isoflurane, mounted in a small amount of
521 halocarbon oil under coverslips with grease spacers. The laser ablation was performed on a Zeiss
522 LSM880 Confocal/Multiphoton Upright Microscope, using a 790 nm two-photon laser at
523 primary dendrites of ddaC neurons in A1 and A3 segments. Animals were recovered on grape
524 juice agar plates following lesion for appropriate times before imaging.

525 ORN axon injury assay was performed on 7-day-old male flies by removing the outer
526 segments of both antennae as described in (MacDonald et al., 2006). The injured males were
527 recovered for 7 days by transferring to fresh yeast-glucose medium every day. To examine
528 Or22a axon degeneration, brains were dissected in PBST (0.2% Triton-X in PBS), fixed in 4%
529 formaldehyde in PBS for 20 min, and then rinsed with PBST three times, 20 minutes each. Then
530 the brains were mounted in SlowFade® Diamond Antifade Mountant (Thermo Fisher Scientific)
531 and imaged using a Leica SP8 microscope with a 40x NA1.3 oil objective.

532 *Long-term time-lapse imaging*

533 Long-term time-lapse imaging at the larval stage was done as described previously (Ji and Han,
534 2020; Sapar et al., 2018). Briefly, a layer of double-sided tape was placed on the coverslip to
535 define the position of PDMS blocks. A small amount of UV glue was added to the groove of
536 PDMS and to the coverslip. Anesthetized larvae were placed on top of the UV glue on the
537 coverslip and then covered by PDMS blocks with the groove side contacting the larva. Glue was
538 then cured by 365nm UV light. The coverslip with attached PDMS and larvae was mounted on
539 an aluminum slide chamber that contained a piece of moisturized Kimwipes (Kimtech Science)
540 paper. Time-lapse imaging was performed on a Leica SP8 confocal equipped with a 40x NA1.3
541 oil objective and a resonant scanner at digital zoom 0.75 and a 3-min or 2-sec interval. For
542 imaging after ablation, larvae were pre-mounted in the imaging chamber and subjected to laser
543 injury. The larvae were then imaged 0.5-1 hours after ablation. For calcium imaging before and
544 immediately after ablation, images were captured on a Zeiss LSM880 Confocal/Multiphoton
545 Upright Microscope on which the ablation was performed.

546 **Image analysis and quantification**

547 Image processing and analyses were done in Fiji/ImageJ. Methods for tracing and measuring
548 C4da neuron dendrite length have been previously described (Poe et al., 2017). Briefly, the
549 images were segmented by Auto Local Threshold and reduced to single pixel skeletons before
550 measurement of skeleton length by pixel distance. The dendrite debris measurement has been
551 described previously (Sapar et al., 2018). Briefly, a dendrite mask was first generated from
552 projected images by Auto Local Threshold in order to create a region of interest (ROI) by
553 dilation to map areas within one-epidermal-cell diameter (40 µm) from dendrites. Dendrite debris
554 within the ROI was converted to binary masks based on fixed thresholds. Different thresholds
555 were used for *ppk-C4-tdTom* and *ppk-Gal4 UAS-CD-tdTom* as they have different brightness.
556 The dendrite pixel area (ADen), debris pixel area (ADeb), and ROI area (AROI) were measured
557 and dendrite coverage ratio was calculated based on the following formula: 100·Adeb·AROI
558 /(AROI- ADen)·ADen. For measuring Lact-GFP, two regions at empty epidermal regions were
559 measured as background levels. TdTom signals on dendrites were used to generate dendrite
560 masks for measurement of GFP within the masks. For kymographs, we used a custom macro
561 based on the Straighten function to extract a strip of pixels centered at the selected dendrite
562 branch. The maximum intensity pixel in the strip at each distance was used to generate a single-
563 pixel line for each time frame. The final kymographs were displayed using the Fire lookup table
564 (LUT).

565 **Statistical Analysis**

566 R was used to conduct statistical analyses and generate graphs. (*$p < 0.05$, **$p < 0.01$, and ***p
567 < 0.001). Statistical significance was set at $p < 0.05$. Data acquisition and quantification were
568 performed non-blinded. Acquisition was performed in ImageJ (batch processing for debris
569 coverage ratio and fragmentation ratio, manually by hand for GFP-Lact binding) and Microsoft
570 Excel. Statistical analyses were performed using R. We used the following R packages: car, stats,
571 multcomp for statistical analysis and ggplot2 for generating graphs. Some graphs were made in
572 Excel using its native plotting functions. For the statistical analysis we ran the following tests,
573 ANOVA (followed by Tukey's HSD) when dependent variable was normally distributed and
574 there was approximately equal variance across groups. When dependent variable was not
575 normally distributed and variance was not equal across groups, we used Kruskal-Wallis

576 (followed by Dunn's test, p-values adjusted with Benjamini-Hochberg method) to test the null
577 hypothesis that assumes that the samples (groups) are from identical populations. To check
578 whether the data fit a normal distribution, we generated qqPlots to analyze whether the residuals
579 of the linear regression model is normally distributed. We used the Levene's test to check for
580 equal variance within groups. The state of neuronal degeneration or fragmentation was compared
581 using the Freeman-Halton extension of Fisher's exact test.

582 *Replication*

583 For all larval and adult imaging experiments, at least 3 biological replications were performed
584 for each genotype and/or condition.

585 **AUTHOR CONTRIBUTIONS**

586 Conceptualization, CH, HJ, MLS, AS; Methodology, CH, HJ, MLS, AS, BW; Investigation, HJ,
587 MLS, AS; Formal Analysis, HJ, MLS, AS; Resources, CH, MLS, HJ, BW, AS; Writing –
588 Original Draft, CH, MLS, HJ, AS; Writing – Review and Editing, CH, MLS, HJ, AS; Funding
589 Acquisition, CH.

590 **ACKNOWLEDGMENTS**

591 We thank Marc Freeman, Yang Xiang, Heather Broihier, and Bloomington Stock Center for fly
592 stocks; Addgene for plasmids; Cornell BRC Imaging facility for access to microscopes (funded
593 by NIH grant S10OD018516); Cornell CSCU for advice on statistics; Mike Goldberg and
594 Fenghua Hu for critical reading and suggestions on the manuscript. This work was supported by
595 a Cornell start-up fund and NIH grants (R01NS099125 and R21OD023824) awarded to C.H.

596 **DECLARATION OF INTEREST**

597 The authors declare no competing interests.

598 **REFERENCE**

599 Akbergenova, Y., Cunningham, K.L., Zhang, Y.V., Weiss, S., and Littleton, J.T. (2018).
600 Characterization of developmental and molecular factors underlying release heterogeneity at
601 Drosophila synapses. Elife *7*.
602 Ali, Y.O., Li-Kroeger, D., Bellen, H.J., Zhai, R.G., and Lu, H.C. (2013). NMNATs,
603 evolutionarily conserved neuronal maintenance factors. Trends Neurosci *36*, 632-640.
604 Avery, M.A., Sheehan, A.E., Kerr, K.S., Wang, J., and Freeman, M.R. (2009). Wld S requires
605 Nmnat1 enzymatic activity and N16-VCP interactions to suppress Wallerian degeneration. J Cell
606 Biol *184*, 501-513.

607 Babetto, E., Beirowski, B., Russler, E.V., Milbrandt, J., and DiAntonio, A. (2013). The Phr1
608 ubiquitin ligase promotes injury-induced axon self-destruction. Cell Rep *3*, 1422-1429.
609 Bratkowski, M., Xie, T., Thayer, D.A., Lad, S., Mathur, P., Yang, Y.S., Danko, G., Burdett,
610 T.C., Danao, J., Cantor, A.*, et al.* (2020). Structural and Mechanistic Regulation of the Pro-
611 degenerative NAD Hydrolase SARM1. Cell Rep *32*, 107999.
612 Canto, C., Menzies, K.J., and Auwerx, J. (2015). NAD(+) Metabolism and the Control of Energy
613 Homeostasis: A Balancing Act between Mitochondria and the Nucleus. Cell Metab *22*, 31-53.
614 Coleman, M.P., and Freeman, M.R. (2010). Wallerian degeneration, wld(s), and nmnat. Annu
615 Rev Neurosci *33*, 245-267.
616 Davies, A.J., Kim, H.W., Gonzalez-Cano, R., Choi, J., Back, S.K., Roh, S.E., Johnson, E.,
617 Gabriac, M., Kim, M.S., Lee, J.*, et al.* (2019). Natural Killer Cells Degenerate Intact Sensory
618 Afferents following Nerve Injury. Cell *176*, 716-728 e718.
619 Di Stefano, M., Nascimento-Ferreira, I., Orsomando, G., Mori, V., Gilley, J., Brown, R.,
620 Janeckova, L., Vargas, M.E., Worrell, L.A., Loreto, A.*, et al.* (2015). A rise in NAD precursor
621 nicotinamide mononucleotide (NMN) after injury promotes axon degeneration. Cell Death Differ
622 *22*, 731-742.
623 Fang, E.F., Lautrup, S., Hou, Y., Demarest, T.G., Croteau, D.L., Mattson, M.P., and Bohr, V.A.
624 (2017). NAD(+) in Aging: Molecular Mechanisms and Translational Implications. Trends Mol
625 Med *23*, 899-916.
626 Farley, J.E., Burdett, T.C., Barria, R., Neukomm, L.J., Kenna, K.P., Landers, J.E., and Freeman,
627 M.R. (2018). Transcription factor Pebbled/RREB1 regulates injury-induced axon degeneration.
628 Proc Natl Acad Sci U S A *115*, 1358-1363.
629 Figley, M.D., Gu, W., Nanson, J.D., Shi, Y., Sasaki, Y., Cunnea, K., Malde, A.K., Jia, X., Luo,
630 Z., Saikot, F.K.*, et al.* (2021). SARM1 is a metabolic sensor activated by an increased
631 NMN/NAD(+) ratio to trigger axon degeneration. Neuron *109*, 1118-1136 e1111.
632 Fourgeaud, L., Traves, P.G., Tufail, Y., Leal-Bailey, H., Lew, E.D., Burrola, P.G., Callaway, P.,
633 Zagorska, A., Rothlin, C.V., Nimmerjahn, A.*, et al.* (2016). TAM receptors regulate multiple
634 features of microglial physiology. Nature *532*, 240-244.
635 Freeman, M.R., Delrow, J., Kim, J., Johnson, E., and Doe, C.Q. (2003). Unwrapping glial
636 biology: Gcm target genes regulating glial development, diversification, and function. Neuron
637 *38*, 567-580.
638 Galloway, D.A., Phillips, A.E.M., Owen, D.R.J., and Moore, C.S. (2019). Phagocytosis in the
639 Brain: Homeostasis and Disease. Front Immunol *10*, 790.
640 George, E., Glass, J., and Griffin, J. (1995). Axotomy-induced axonal degeneration is mediated
641 by calcium influx through ion-specific channels. The Journal of Neuroscience *15*, 6445-6452.
642 Gerdts, J., Brace, E.J., Sasaki, Y., DiAntonio, A., and Milbrandt, J. (2015). SARM1 activation
643 triggers axon degeneration locally via NAD(+) destruction. Science *348*, 453-457.
644 Gerdts, J., Summers, D.W., Milbrandt, J., and DiAntonio, A. (2016). Axon Self-Destruction:
645 New Links among SARM1, MAPKs, and NAD+ Metabolism. Neuron *89*, 449-460.
646 Han, C., Jan, L.Y., and Jan, Y.N. (2011). Enhancer-driven membrane markers for analysis of
647 nonautonomous mechanisms reveal neuron-glia interactions in Drosophila. Proc Natl Acad Sci U
648 S A *108*, 9673-9678.
649 Han, C., Song, Y., Xiao, H., Wang, D., Franc, N.C., Jan, L.Y., and Jan, Y.N. (2014). Epidermal
650 cells are the primary phagocytes in the fragmentation and clearance of degenerating dendrites in
651 Drosophila. Neuron *81*, 544-560.

652 Ji, H., and Han, C. (2020). LarvaSPA, A Method for Mounting Drosophila Larva for Long-Term
653 Time-Lapse Imaging. J Vis Exp.
654 Jiang, Y., Liu, T., Lee, C.H., Chang, Q., Yang, J., and Zhang, Z. (2020). The NAD(+)-mediated
655 self-inhibition mechanism of pro-neurodegenerative SARM1. Nature *588*, 658-663.
656 Kanamori, T., Kanai, M.I., Dairyo, Y., Yasunaga, K., Morikawa, R.K., and Emoto, K. (2013).
657 Compartmentalized calcium transients trigger dendrite pruning in Drosophila sensory neurons.
658 Science *340*, 1475-1478.
659 Koreman, G.T., Xu, Y., Hu, Q., Zhang, Z., Allen, S.E., Wolfner, M.F., Wang, B., and Han, C.
660 (2021). Upgraded CRISPR/Cas9 tools for tissue-specific mutagenesis in Drosophila. Proc Natl
661 Acad Sci U S A *118*.
662 Leventis, P.A., and Grinstein, S. (2010). The distribution and function of phosphatidylserine in
663 cellular membranes. Annu Rev Biophys *39*, 407-427.
664 Lin, J.B., Kubota, S., Ban, N., Yoshida, M., Santeford, A., Sene, A., Nakamura, R., Zapata, N.,
665 Kubota, M., Tsubota, K.*, et al.* (2016). NAMPT-Mediated NAD(+) Biosynthesis Is Essential for
666 Vision In Mice. Cell Rep *17*, 69-85.
667 Liu, H.W., Smith, C.B., Schmidt, M.S., Cambronne, X.A., Cohen, M.S., Migaud, M.E., Brenner,
668 C., and Goodman, R.H. (2018). Pharmacological bypass of NAD(+) salvage pathway protects
669 neurons from chemotherapy-induced degeneration. Proc Natl Acad Sci U S A.
670 MacDonald, J.M., Beach, M.G., Porpiglia, E., Sheehan, A.E., Watts, R.J., and Freeman, M.R.
671 (2006). The Drosophila cell corpse engulfment receptor Draper mediates glial clearance of
672 severed axons. Neuron *50*, 869-881.
673 Mack, T.G., Reiner, M., Beirowski, B., Mi, W., Emanuelli, M., Wagner, D., Thomson, D.,
674 Gillingwater, T., Court, F., Conforti, L.*, et al.* (2001). Wallerian degeneration of injured axons
675 and synapses is delayed by a Ube4b/Nmnat chimeric gene. Nat Neurosci *4*, 1199-1206.
676 Mazaheri, F., Breus, O., Durdu, S., Haas, P., Wittbrodt, J., Gilmour, D., and Peri, F. (2014).
677 Distinct roles for BAI1 and TIM-4 in the engulfment of dying neurons by microglia. Nat
678 Commun *5*, 4046.
679 Miller, B.R., Press, C., Daniels, R.W., Sasaki, Y., Milbrandt, J., and DiAntonio, A. (2009). A
680 dual leucine kinase-dependent axon self-destruction program promotes Wallerian degeneration.
681 Nat Neurosci *12*, 387-389.
682 Nandrot, E.F., Anand, M., Almeida, D., Atabai, K., Sheppard, D., and Finnemann, S.C. (2007).
683 Essential role for MFG-E8 as ligand for alphavbeta5 integrin in diurnal retinal phagocytosis.
684 Proc Natl Acad Sci U S A *104*, 12005-12010.
685 Neukomm, L.J., Burdett, T.C., Seeds, A.M., Hampel, S., Coutinho-Budd, J.C., Farley, J.E.,
686 Wong, J., Karadeniz, Y.B., Osterloh, J.M., Sheehan, A.E.*, et al.* (2017). Axon Death Pathways
687 Converge on Axundead to Promote Functional and Structural Axon Disassembly. Neuron *95*, 78-
688 91 e75.
689 Nomura-Komoike, K., Saitoh, F., and Fujieda, H. (2020). Phosphatidylserine recognition and
690 Rac1 activation are required for Muller glia proliferation, gliosis and phagocytosis after retinal
691 injury. Sci Rep *10*, 1488.
692 Osterloh, J.M., Yang, J., Rooney, T.M., Fox, A.N., Adalbert, R., Powell, E.H., Sheehan, A.E.,
693 Avery, M.A., Hackett, R., Logan, M.A.*, et al.* (2012). dSarm/Sarm1 is required for activation of
694 an injury-induced axon death pathway. Science *337*, 481-484.
695 Poe, A.R., Tang, L., Wang, B., Li, Y., Sapar, M.L., and Han, C. (2017). Dendritic space-filling
696 requires a neuronal type-specific extracellular permissive signal in Drosophila. Proc Natl Acad
697 Sci U S A *114*, E8062-E8071.

698 Poe, A.R., Wang, B., Sapar, M.L., Ji, H., Li, K., Onabajo, T., Fazliyeva, R., Gibbs, M., Qiu, Y.,
699 Hu, Y., *et al.* (2019). Robust CRISPR/Cas9-Mediated Tissue-Specific Mutagenesis Reveals
700 Gene Redundancy and Perdurance in Drosophila. Genetics *211*, 459-472.
701 Raiders, S., Black, E.C., Bae, A., MacFarlane, S., Klein, M., Shaham, S., and Singhvi, A. (2021).
702 Glia actively sculpt sensory neurons by controlled phagocytosis to tune animal behavior. Elife
703 *10*.
704 Sapar, M.L., and Han, C. (2019). Die in pieces: How Drosophila sheds light on neurite
705 degeneration and clearance. J Genet Genomics *46*, 187-199.
706 Sapar, M.L., Ji, H., Wang, B., Poe, A.R., Dubey, K., Ren, X., Ni, J.Q., and Han, C. (2018).
707 Phosphatidylserine Externalization Results from and Causes Neurite Degeneration in Drosophila.
708 Cell Rep *24*, 2273-2286.
709 Sasaki, Y., Nakagawa, T., Mao, X., DiAntonio, A., and Milbrandt, J. (2016). NMNAT1 inhibits
710 axon degeneration via blockade of SARM1-mediated NAD(+) depletion. Elife *5*.
711 Shacham-Silverberg, V., Sar Shalom, H., Goldner, R., Golan-Vaishenker, Y., Gurwicz, N.,
712 Gokhman, I., and Yaron, A. (2018). Phosphatidylserine is a marker for axonal debris engulfment
713 but its exposure can be decoupled from degeneration. Cell Death Dis *9*, 1116.
714 Shen, C., Vohra, M., Zhang, P., Mao, X., Figley, M.D., Zhu, J., Sasaki, Y., Wu, H., DiAntonio,
715 A., and Milbrandt, J. (2021). Multiple domain interfaces mediate SARM1 autoinhibition. Proc
716 Natl Acad Sci U S A *118*.
717 Sievers, C., Platt, N., Perry, V.H., Coleman, M.P., and Conforti, L. (2003). Neurites undergoing
718 Wallerian degeneration show an apoptotic-like process with Annexin V positive staining and loss
719 of mitochondrial membrane potential. Neurosci Res *46*, 161-169.
720 Suzuki, J., Umeda, M., Sims, P.J., and Nagata, S. (2010). Calcium-dependent phospholipid
721 scrambling by TMEM16F. Nature *468*, 834-838.
722 Tanaka, K., Fujimura-Kamada, K., and Yamamoto, T. (2011). Functions of phospholipid
723 flippases. J Biochem *149*, 131-143.
724 Tao, J., and Rolls, M.M. (2011). Dendrites have a rapid program of injury-induced degeneration
725 that is molecularly distinct from developmental pruning. J Neurosci *31*, 5398-5405.
726 Tung, T.T., Nagaosa, K., Fujita, Y., Kita, A., Mori, H., Okada, R., Nonaka, S., and Nakanishi, Y.
727 (2013). Phosphatidylserine recognition and induction of apoptotic cell clearance by Drosophila
728 engulfment receptor Draper. J Biochem *153*, 483-491.
729 Vargas, M.E., Yamagishi, Y., Tessier-Lavigne, M., and Sagasti, A. (2015). Live Imaging of
730 Calcium Dynamics during Axon Degeneration Reveals Two Functionally Distinct Phases of
731 Calcium Influx. J Neurosci *35*, 15026-15038.
732 Verdin, E. (2015). NAD(+) in aging, metabolism, and neurodegeneration. Science *350*, 1208-
733 1213.
734 Waller, A. (1850). Experiments on the Section of the Glossopharyngeal and Hypoglossal Nerves
735 of the Frog, and Observations of the Alterations Produced Thereby in the Structure of Their
736 Primitive Fibres. Philosophical Transactions of the Royal Society of London *140*, 423-429.
737 Wang, J., Zhai, Q., Chen, Y., Lin, E., Gu, W., McBurney, M.W., and He, Z. (2005). A local
738 mechanism mediates NAD-dependent protection of axon degeneration. J Cell Biol *170*, 349-355.
739 Wen, Y., Parrish, J.Z., He, R., Zhai, R.G., and Kim, M.D. (2011). Nmnat exerts neuroprotective
740 effects in dendrites and axons. Mol Cell Neurosci *48*, 1-8.
741 Williams, P.R., Marincu, B.N., Sorbara, C.D., Mahler, C.F., Schumacher, A.M., Griesbeck, O.,
742 Kerschensteiner, M., and Misgeld, T. (2014). A recoverable state of axon injury persists for
743 hours after spinal cord contusion in vivo. Nat Commun *5*, 5683.

744 Witte, M.E., Schumacher, A.M., Mahler, C.F., Bewersdorf, J.P., Lehmitz, J., Scheiter, A.,
745 Sanchez, P., Williams, P.R., Griesbeck, O., Naumann, R.*, et al.* (2019). Calcium Influx through
746 Plasma-Membrane Nanoruptures Drives Axon Degeneration in a Model of Multiple Sclerosis.
747 Neuron *101*, 615-624 e615.
748 Xiong, X., Hao, Y., Sun, K., Li, J., Li, X., Mishra, B., Soppina, P., Wu, C., Hume, R.I., and
749 Collins, C.A. (2012). The Highwire ubiquitin ligase promotes axonal degeneration by tuning
750 levels of Nmnat protein. PLoS Biol *10*, e1001440.
751 Yang, J., Wu, Z., Renier, N., Simon, D.J., Uryu, K., Park, D.S., Greer, P.A., Tournier, C., Davis,
752 R.J., and Tessier-Lavigne, M. (2015). Pathological axonal death through a MAPK cascade that
753 triggers a local energy deficit. Cell *160*, 161-176.
754 Zhai, R.G., Cao, Y., Hiesinger, P.R., Zhou, Y., Mehta, S.Q., Schulze, K.L., Verstreken, P., and
755 Bellen, H.J. (2006). Drosophila NMNAT maintains neural integrity independent of its NAD
756 synthesis activity. PLoS Biol *4*, e416.
757 Zhai, R.G., Rizzi, M., and Garavaglia, S. (2009). Nicotinamide/nicotinic acid mononucleotide
758 adenylyltransferase, new insights into an ancient enzyme. Cell Mol Life Sci *66*, 2805-2818.
759

760 **VIDEO LEGEND**

761 **Video 1. GFP-Lact labeling of degenerating *Nmnat* KO dendrites, related to Figure 2.**

762 Time-lapse movie of GFP-Lact labeling on distal dendrites of a *Nmnat* KO C4da neuron before
763 and during degeneration. Imaging started around 96 hours AEL. *Dcg-Gal4* drives GFP-Lact
764 expression in both fat bodies (not shown) and hemocytes (mobile cells in the GFP-Lact channel).
765 Timestamp is relative to the first frame, with a 3-min interval between each frame.

766 **Video 2. Dendrite dynamics of *Nmnat* KO neurons in *drpr* mutant larvae, related to Figure**
767 **2.**

768 Time-lapse movie of dendrites of a *Nmnat* KO neuron exhibiting dynamic extension and
769 retraction behaviors in a *drpr* mutant larva. Imaging started around 120 hours AEL. Timestamp
770 is relative to the first frame, with a 3-min interval between each frame.

771 **Video 3. Membrane rupture of injured dendrites, related to Figure 7.**

772 Time-lapse movie of laser-injured C4da dendrites from 1 to 11 hours AI. Reconstituted GFP is
773 from extracellular GFP$(11)_{x7}$ entering the dendrites and myr-tdTom-GFP(1-10) attached to the
774 inner leaflet of dendritic membrane. Timestamp is relative to the first frame, with a 3-min
775 interval between each frame.

776 **Video 4. Cytoplasmic calcium dynamics in uninjured wildtype dendrites, related to Figure**
777 **8.**

778 Time-lapse movie of an uninjured wildtype C4da neuron showing low baseline GCaMP6s
779 signals and occasional local rises in dendrites. Timestamp is relative to the first frame, with a 3-
780 min interval between each frame.

781 **Video 5. Cytoplasmic calcium dynamics in dendrites of *Nmnat* KO neurons, related to**
782 **Figure 8.**

783 Time-lapse movie of a *Nmnat* KO C4da neuron showing calcium dynamics in uninjured
784 dendrites. Timestamp is relative to the first frame, with a 3-min interval between each frame.

785 **Video 6. Calcium dynamics in injured wildtype dendrites, related to Figure 8.**

786 Time-lapse movie of laser-injured C4da dendrites from 1 to 11 hrs AI showing calcium
787 dynamics in both severed dendrites and those attached to the soma. Timestamp is relative to the
788 first frame, with a 3-min interval between each frame.

789 **Video 7. AV-mCard labeling and calcium dynamics of injured dendrites, related to Figure**
790 **8.**

791 Time-lapse movie of laser-injured C4da dendrites from 1 to 6 hrs AI showing labeling of injured
792 dendrites by the PS sensor AV-mCard and GCaMP6s signals. Timestamp is relative to the first
793 frame, with a 3-min interval between each frame.

794 **Video 8. Calcium dynamics in injured Wld^S OE dendrites, related to Figure 8.**

795 Time-lapse movie of laser-injured Wld^S OE C4da dendrites from 1 to 13 hours AI showing
796 GCaMP6s signals in severed dendrites. Timestamp is relative to the first frame, with a 3-min
797 interval between each frame.

798 **Video 9. Calcium dynamics in injured wildtype dendrites with a higher temporal**
799 **resolution, related to Figure 8.**

800 High temporal-resolution time-lapse movie of laser-injured wildtype C4da dendrites around 1 hr
801 AI showing calcium dynamics. Timestamp is relative to the first frame, with a 2-sec interval
802 between each frame.

803 **Video 10. Calcium dynamics in injured Wld^S OE dendrites at a higher temporal resolution,**
804 **related to Figure 8.**

805 High temporal-resolution time-lapse movie of laser-injured Wld^S OE C4da dendrites around 2
806 hrs AI showing calcium dynamics. Timestamp is relative to the first frame, with a 2-sec interval
807 between each frame.

808 **Video 11. Irregular and infrequent cytoplasmic calcium flashes in injured Wld^S OE**
809 **dendrites at a higher temporal resolution, related to Figure 8.**

810 High temporal-resolution time-lapse movie of laser-injured Wld^S OE C4da dendrites around 2
811 hrs AI showing irregular and infrequent GCaMP6s signals in severed dendrites. Timestamp is
812 relative to the first frame, with a 2-sec interval between each frame.

813 **Video 12. Calcium dynamics in injured *axed* KO dendrites, related to Figure 8.**

814 Time-lapse movie of laser-injured *axed* KO C4da dendrites from 0.5 to 5.5 hours AI showing
815 GCaMP6s signals in severed dendrites. Timestamp is relative to the first frame, with a 3-min
816 interval between each frame.

817 **Video 13. Calcium dynamics in injured *axed* KO dendrites at a higher temporal resolution,**
818 **related to Figure 8.**

819 High temporal-resolution time-lapse movie of laser-injured *axed* KO C4da dendrites around 10
820 min AI showing calcium dynamics. Timestamp is relative to the first frame, with a 2-sec interval
821 between each frame.